CHEMISTRY
A EUROPEAN JOURNAL

DOI: 10.1002/chem.200901581

A ^{93}Nb Solid-State NMR and Density Functional Theory Study of Four- and Six-Coordinate Niobate Systems

John V. Hanna,*[a] Kevin J. Pike,[a] Thibault Charpentier,[b] Thomas F. Kemp,[a] Mark E. Smith,[a] Bryan E. G. Lucier,[c] Robert W. Schurko,[c] and Lindsay S. Cahill[a]

Abstract: A variable B_0 field static (broadline) NMR study of a large suite of niobate materials has enabled the elucidation of high-precision measurement of ^{93}Nb NMR interaction parameters such as the isotropic chemical shift (δ_{iso}), quadrupole coupling constant and asymmetry parameter (C_Q and η_Q), chemical shift span/anisotropy and skew/asymmetry ($\Omega/\Delta\delta$ and κ/η_δ) and Euler angles (α, β, γ) describing the relative orientation of the quadrupolar and chemical shift tensorial frames. These measurements have been augmented with ab initio DFT calculations by using WIEN2k and NMR-CASTEP codes, which corroborate these reported values. Unlike previous assertions made about the inability to detect CSA (chemical shift anisotropy) contributions from Nb^V in most oxo environments, this study emphasises that a thorough variable B_0 approach coupled with the VOCS (variable offset cumulative spectroscopy) technique for the acquisition of undistorted broad ($-1/2 \leftrightarrow +1/2$) central transition resonances facilitates the unambiguous observation of both quadrupolar and CSA contributions within these ^{93}Nb broadline data. These measurements reveal that the ^{93}Nb electric field gradient tensor is a particularly sensitive measure of the immediate and extended environments of the Nb^V positions, with C_Q values in the 0 to >80 MHz range being measured; similarly, the δ_{iso} (covering an approximately 250 ppm range) and Ω values (covering a 0 to approximately 800 ppm range) characteristic of these niobate systems are also sensitive to structural disposition. However, their systematic rationalisation in terms of the Nb–O bond angles and distances defining the immediate Nb^V oxo environment is complicated by longer-range influences that usually involve other heavy elements comprising the structure. It has also been established in this study that the best computational method(s) of analysis for the ^{93}Nb NMR interaction parameters generated here are the all-electron WIEN2k and the gauge included projector augmented wave (GIPAW) NMR-CASTEP DFT approaches, which account for the short- and long-range symmetries, periodicities and interaction-potential characteristics for all elements (and particularly the heavy elements) in comparison with Gaussian 03 methods, which focus on terminated portions of the total structure.

Keywords: ab initio calculations · niobium · NMR spectroscopy · solid-state NMR spectroscopy · static line shapes

Introduction

Group V chemistry has attracted growing attention mainly owing to the unique and flexible attributes exhibited by niobium iono–covalent coordination properties, which are more pronounced than its Group V counterparts vanadium and tantalum.[1–7] It has been demonstrated by many authors that the introduction of Nb^V merely at the dopant level significantly contributes to the catalytic activity, stability and selectivity of functional materials such as catalysts, catalytic supports and microporous and mesoporous ion-exchange systems.[3,4,8,9] Favourable properties such as catalytic activity, selectivity and stability within low pH regimes have been exhibited by hydrated niobium oxides ($Nb_2O_5 \cdot xH_2O$) and

[a] Dr. J. V. Hanna, Dr. K. J. Pike, Dr. T. F. Kemp, Prof. M. E. Smith, Dr. L. S. Cahill
Department of Physics, University of Warwick
Gibbet Hill Rd., Coventry CV4 7AL (UK)
Fax: (+44) 2476-150954
E-mail: j.v.hanna@warwick.ac.uk

[b] Dr. T. Charpentier
Commissariat à l'Energie Atomique, IRAMIS-SIS2M
Laboratoire de Structure et Dymanique par Résonance Magnétique (LSDRM)
F-91191 Gif-sur-Yvette Cedex (France)

[c] B. E. G. Lucier, Prof. R. W. Schurko
Department of Chemistry & Biochemistry
University of Windsor, Windsor, Ontario N9B 3P4 (Canada)

niobium phosphates, with niobium(V) oxides and mixed oxides frequently underpinning metal supports and combined metal–oxide catalyst systems.[2,4,10,11] Solid-state niobate chemistry also plays a crucial role in the piezoelectric phases formed by $Pb(Mg_{1/3}Nb_{2/3})O_3$ (PMN)[12,13] and by the solid solutions $(1-x)Pb(Mg_{1/3}Nb_{2/3})O_3{\cdot}xPbTiO_3$ (PMN/PT)[14–16] and $(1-x)Pb(Mg_{1/3}Nb_{2/3})O_3{\cdot}xPb(Sc_{1/2}Nb_{1/2})O_3$ (PMN/PSN)[17–19] comprising the perovskite relaxor ferroelectric families of materials. Furthermore, significant advances in glass fabrication and utility have been associated with the incorporation of Nb^V into disordered oxide networks. Ternary glass systems such as $Nb_2O_5/NaPO_3/Na_2B_4O_7$ have been studied[20,21] and theoretically modelled[22,23] to understand the marked non-linear optical response obtained from these transparent materials, and niobiophosphate glasses have displayed improved properties over conventional phosphate analogues, particularly for hosting rare-earth elements thus targeting optical applications,[24–26] as well as for hosting lanthanides and actinides in nuclear waste immobilisation scenarios.[27]

Despite the demonstrated importance of Nb^V in the speciation and function of this broad range of materials, ^{93}Nb solid-state NMR spectroscopy has not been a prominent method of characterisation, with only a limited number of studies having reported the use of ^{93}Nb static (broadline, stationary samples) and magic-angle-spinning (MAS) NMR methods to complement other characterisation techniques.[12–19,28–35] The large gyromagnetic ratio ($\gamma = 6.567 \times 10^7\ rad\,s^{-1}T^{-1}$) and 100% natural abundance makes ^{93}Nb the fourth most receptive nucleus in the NMR periodic table; however, this spin $I = 9/2$ nucleus also possesses a large quadrupole moment ($Q = -32 \times 10^{-30}\ m^2$), which introduces a dominant second-order quadrupolar broadening to the central transition ($-1/2 \leftrightarrow +1/2$) spectra. In addition, ^{93}Nb exhibits a large chemical shift range (typically ~4000 ppm), which can promote significant chemical shift dispersion broadening of static and MAS resonances from the studies of disordered systems. The lack of an adequate suite of Nb^V-containing model compounds and difficulties with characterising niobate systems (either with chemical shift or quadrupolar parameters) through ab initio DFT calculations have rendered the routine introduction of ^{93}Nb solid-state NMR techniques problematic. To date, only one study has attempted to compare a DFT analysis with an experimentally acquired ^{93}Nb dataset; this pertained to Nb^I and Nb^V half-sandwich cyclopentadienyl complexes with the restricted Hartree–Fock (RHF) and hybrid DFT (B3LYP) Gaussian 03 calculations, which produced reasonably correlated results.[33] Previous studies have attempted to analyse ^{93}Nb second-order quadrupolar broadened central transition line shapes from suites of niobates and to use the resultant isotropic chemical shift (δ_{iso}) data to map predictive shift ranges.[28,29] However, the incomplete analysis of this lineshape data has resulted in low-precision values of δ_{iso}, C_Q, η_Q, Ω and κ (or $\Delta\delta$ and η_δ) being reported, and some of the broader proposed chemical shift ranges may need to be revised. Moreover, the precision inherent in these previously reported ^{93}Nb NMR interaction parameters is not suitable for correlation against DFT calculated values, and a more rigorous approach to obtain second-order broadened ($-1/2 \leftrightarrow +1/2$) central transition data for these niobate systems must be undertaken to assess the real predictive capability of DFT calculations for heavier elements such as niobium.

This study aims to establish an accurate basis for the measurement of ^{93}Nb NMR interaction parameters (δ_{iso}, C_Q, η_Q, Ω and κ (or $\Delta\delta$ and η_δ) and α, β and γ) by characterising the electric field gradient (EFG) and chemical shift (CS) tensors in fundamental niobate systems. Precise data can be elucidated only if undistorted and complete line shapes from broad second-order quadrupole/chemical shift anisotropy dominated central transition resonances are acquired, and recourse to frequency offset subspectral addition techniques such as VOCS (variable offset cumulative spectroscopy)[36–38] must be taken. These reconstructed line shapes will facilitate a clearly defined deconvolution of these line-broadening contributions and permit further analyses to be undertaken with greater confidence. Given the convoluted nature of the contributions characterising these niobate resonances, the only way to constrain and elucidate each NMR interaction tensor effectively is to obtain variable B_0 field data over the greatest range available. These experimental measurements will be positioned against the latest DFT computational methods such as WIEN2k, NMR-CASTEP and Gaussian 03 to assess their potential for accurately predicting ^{93}Nb NMR parameters from structures containing one or more heavy elements. Conventional DFT codes such as WIEN2k and NMR-CASTEP are well suited for handling periodic structures such as those exhibited by niobates, and these are utilised for the computation and prediction of ^{93}Nb NMR quadrupolar (C_Q, η_Q) and chemical shift (δ_{iso}, Ω and κ (or $\Delta\delta$ and η_δ)) interaction parameters from which correlations between experiment and calculation will be drawn. Further comparison will be made with computations by using the Gaussian 03 methodology, which focuses on terminated portions of the total periodic structure to assess further whether these less time-consuming calculations can accurately describe NMR interaction tensors in heavy-element networks.

Experimental Section

Sample preparation: The niobates $YNbO_4$, $LaNbO_4$, $MgNb_2O_6$, $Mg_4Nb_2O_6$, La_3NbO_7, $BiNbO_4$, Bi_3NbO_7, $Cd_2Nb_2O_7$, $CaNb_2O_6$ and $CsBiNb_2O_7$ studied in this work were synthesised according to previously reported methods.[39–48] The tin niobate systems such as $SnNb_2O_6$ and $Sn_2Nb_2O_7$ also studied here were commercially produced samples supplied by Johnson Matthey UK, and alkali perovskite systems such as $LiNbO_3$ (93-0338), $NaNbO_3$ (93-1057) and $KNbO_3$ (93-4117) were commercially purchased products from Strem Chemical Co., which exhibited nominal purities of >99.99%. The crystallinity and purity of all niobate samples were checked with additional characterisation methods such as XRD and SEM prior to NMR study.

^{93}Nb static and MAS NMR acquisition: Static broadline ^{93}Nb NMR data were acquired at ambient temperatures on 4.7, 7.1, 9.4, 14.1 and 18.8 T

systems by using Chemagnetics CMX-200, Varian Infinity Plus-300, Bruker DSX-400, Bruker Avance II+-600 and Varian CMX Infinity Plus-800 spectrometers operating at ^{93}Nb Larmor frequencies of 49.95, 73.74, 97.83, 146.72 and 195.54 MHz, respectively. These measurements were performed by using Bruker 5/7.5 mm static horizontal solenoid design probes at 4.7, 7.1, 9.4 and 14.1 T, and with a home-built, balanced-circuit design 5/7.5 mm static horizontal solenoid probe at 18.8 T. All static ^{93}Nb data were acquired with the solid echo θ–τ–θ–τ–(acquire) ($\theta \approx \pi/4$) experiment with an extended phase cycle to capture undistorted echoes with minimal influences from residual echo tails and finite pulse widths.[49,50] Previously reported studies on the application of spin-echo experiments to half-integer quadrupolar nuclei have demonstrated that the predominant complication of this analysis is the strong nutational phenomena influenced by the radio-frequency (RF) field strength ν_{rf} and the orientation-dependent frequency $\nu_Q(\theta,\phi)$ defining the first-order quadrupolar interaction.[50–55] Only in the extreme limiting cases in which $\nu_{rf} \gg \nu_Q(\theta,\phi)$ and $\nu_{rf} \ll \nu_Q(\theta,\phi)$ does the excitation of a powder line shape assume independence from any crystallite orientation. For a spin $I=9/2$ nucleus such as ^{93}Nb, the strong irradiation condition is virtually impossible to satisfy and the weak ν_{rf} regime becomes the only option available to obtain undistorted ($-1/2 \leftrightarrow +1/2$) central transition data. However, this approach limits the effective bandwidth of each solid echo experiment. Non-selective (solution) $\pi/2$ pulse widths of 8–10 μs were calibrated on a saturated $K[NbCl_6]/CH_3CN$ solution from which selective (solid) θ pulses of 0.8–1.0 μs were employed in the solid echo measurements. The τ delay was 20 μs and the relaxation delay between transients was 2 s. Acquired ^{93}Nb data from materials characterised by sufficiently small quadrupole interactions (i.e., narrower central transition resonance breadths across the base, $\Delta\nu <$ approximately 120 kHz) were obtained with single solid echo experiments. Measurements on systems with larger quadrupole interactions (i.e., larger central transition resonance breadths across the base, $\Delta\nu >$ approximately 120 kHz) required the use of the VOCS[36–38] technique because it is not feasible to excite these larger central transition resonances uniformly with a single static ^{93}Nb experiment under the constraint of the $\nu_{rf} \ll \nu_Q(\theta,\phi)$ pulse condition. This method entails the stepping of the solid echo experiment through a suitable number of carrier frequencies, typically separated by offsets of 100 kHz, to excite the full width of each central transition resonance uniformly. The subsequent coaddition of these subspectra (after shifting to a common spectral reference) provides an undistorted representation of each broad line shape. Three examples of this approach are given in Figure 1 a–c for $YNbO_4$, $CaNb_2O_6$ and $MgNb_2O_6$, respectively. All ^{93}Nb isotropic chemical shifts (δ_{iso}) are directly referenced to the above-mentioned saturated $K[NbCl_6]/CH_3CN$ primary standard, which was assigned to $\delta = 0.0$ ppm. MAS ^{93}Nb NMR data were acquired at ambient temperature on 11.7, 14.1 and 18.8 T systems by using Bruker Avance II-500, Bruker Avance II+-600 and Varian CMX Infinity Plus-800 spectrometers operating at ^{93}Nb Larmor frequencies of 122.65, 146.72 and 195.54 MHz, respectively. The MAS NMR measurements at 11.7 T were performed by using a Bruker 2.5 mm fast MAS probe capable of MAS frequencies (ν_r) of up to ~30 kHz, whereas those at 14.1 T used a custom-built 1.8 mm fast MAS probe capable of MAS frequencies of up to ~40 kHz. High-field MAS NMR measurements at 18.8 T utilised a Varian 2.5 mm fast MAS probe delivering MAS frequencies of up to ~30 kHz. At each field, data were acquired with a conventional single-pulse experiment; a non-selective (solution) $\pi/2$ pulse time of 10 μs was calibrated on a saturated $K[NbCl_6]/CH_3CN$ solution from which a selective (solid) θ pulse of 0.8 μs was employed in the single-pulse measurements. A recycle delay of 2 s was used for MAS measurements and all ^{93}Nb isotropic chemical shifts (δ_{iso}) are directly referenced to the $K[NbCl_6]/CH_3CN$ primary standard at $\delta = 0.0$ ppm.

Two-dimensional, triple-quantum MAS (2D 3QMAS) ^{93}Nb NMR data were acquired at 11.7 T on a Bruker Avance II-500 spectrometer operating at a ^{93}Nb Larmor frequency of 122.17 MHz. 2D 3QMAS spectra were obtained by using the amplitude modulated Z-filter experiment (p_1–t_1(3Q evolution)–p_2–τ–p_3–t_2(acquire)).[56] The optimised pulse lengths of the triple quantum excitation (p_1) and reconversion (p_2) pulses were $p_1 = 2.4$ μs and $p_2 = 0.8$ μs, respectively, implemented with an RF field of 125 kHz, whereas the soft $\pi/2$ Z-filter (p_3) pulse was set to 4 μs, which was delivered with an RF field of 15 kHz. 2D 3QMAS measurements on disordered pyrochlore systems such as Bi_3NbO_7 and $Sn_2Nb_2O_7$ required 128 t_1 increments of 6 μs dwell time acquired with 216 and 720 transients per t_1 slice, respectively. For ordered systems such as $BiNbO_4$, 64 rotor synchronised t_1 increments of 32 μs separation (corresponding to $\nu_r = 31.25$ kHz) were acquired with 180 transients per t_1 slice. In all 3QMAS measurements $\nu_r = 31.25$ kHz, the Z-filter τ period was set to one rotor period of 32 μs and the recycle delay was 0.5 s.

^{93}Nb static and MAS NMR data simulation and processing: All solid echo static line shapes were simulated with the Bruker TOPSPIN, QUASAR[57,58] and WSOLIDS[59] line-shape simulation packages equipped to handle convoluted quadrupolar/chemical shift anisotropy (CSA) dominated line shapes. These packages described each line shape with nine NMR interaction parameters, which included the isotropic chemical shift (δ_{iso}) defined in [Eq. (1)], the quadrupole coupling constant (C_Q) and quadrupole asymmetry parameter (η_Q) defined in [Eq. (2)] and [Eq.(3)], the CSA ($\Delta\delta$) and chemical shift asymmetry parameter (η_δ) (in the Haeberlen convention) defined in [Eq. (4)] and [Eq. (5)], and the chemical shift span (CSS, Ω) and chemical shift skew (κ) (in the Herzfeld-Berger convention) defined in [Eq. (6)] and [Eq. (7)], respectively.

$$\delta_{iso} = (\delta_{11} + \delta_{22} + \delta_{33})/3 \quad (1)$$

$$C_Q = e^2qQ/h = eQV_{33}/h, \quad |V_{33}| \geq |V_{22}| \geq |V_{11}| \quad (2)$$

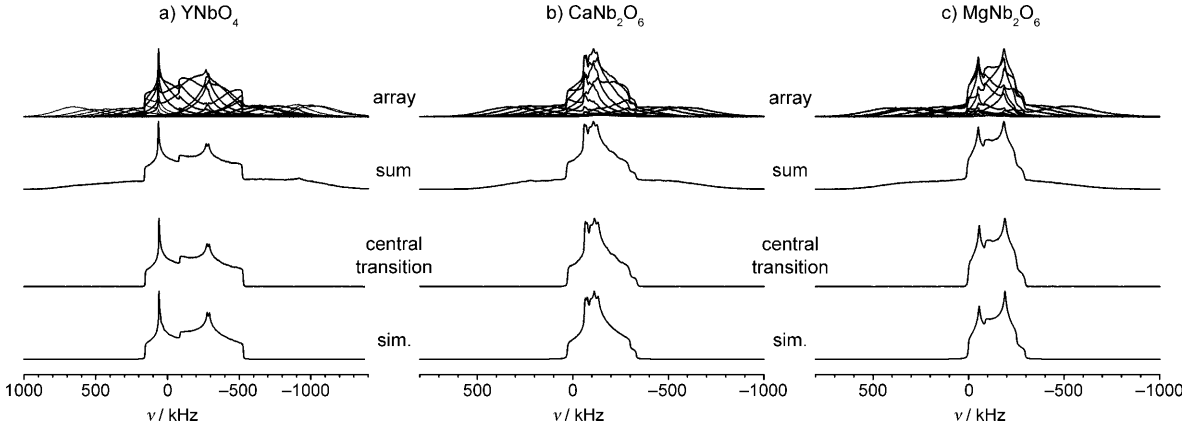

Figure 1. A demonstration of VOCS arrayed data for the acquisition of ^{93}Nb ($-1/2 \leftrightarrow +1/2$) central transition spectra for a) $YNbO_4$, b) $CaNb_2O_6$ and c) $MgNb_2O_6$ at a B_0 field of 9.4 T. Sim. = simulated.

$$\eta_Q = (V_{11}-V_{22})/V_{33}, \quad (1 \geq \eta_Q \geq 0) \tag{3}$$

$$\Delta\delta = \delta_{33}-1/2(\delta_{11}+\delta_{22}) = 3/2(\delta_{33}-\delta_{iso}), \quad |\delta_{33}-\delta_{iso}| \geq |\delta_{11}-\delta_{iso}| \geq |\delta_{22}-\delta_{iso}| \tag{4}$$

$$\eta_\delta = (\delta_{22}-\delta_{11})/(\delta_{33}-\delta_{iso}), \quad (1 \geq \eta_\delta \geq 0) \tag{5}$$

$$\Omega = (\delta_{11}-\delta_{33}), \quad \delta_{11} \geq \delta_{22} \geq \delta_{33} \tag{6}$$

$$\kappa = 3(\delta_{22}-\delta_{iso})/(\delta_{11}-\delta_{33}), \quad (1 \geq \kappa \geq -1) \tag{7}$$

The Euler angles (α, β, γ) describe the relative orientation of the EFG and CS tensors and $\Delta\nu$ is a Gaussian/Lorentzian line-broadening factor. An accurate deconvolution and elucidation of these parameters can only be achieved if the data is constrained by a variable B_0 approach. The collective data for each niobate system were simulated by cycling through each ^{93}Nb spectrum acquired at the various B_0 fields until complete consistency in the NMR interaction parameters was achieved and the concomitant residual-sum-of-squares error in each simulation was less than ~5%. It should be noted that the chemical shift output from these simulation packages varies in its format. Both WSOLIDS and TOPSPIN allow the chemical shift information to be expressed within both conventions mentioned above, and by the more basic shift tensor element format (i.e., δ_{11}, δ_{22}, δ_{33}), whereas QUASAR adopts a hybrid scheme by using the CCS (Ω) and the asymmetry parameter (η_δ). This must be reconciled against the basic shielding tensor element format (σ_{11}, σ_{22}, σ_{33}) adopted in the CASTEP DFT output introduced below.

All 2D ^{93}Nb 3QMAS data were Fourier transformed, sheared and referenced in the indirect (F1) dimension according to conventional Bruker TOPSPIN algorithms. To extract the underlying distribution of NMR parameters (denoted $P(\delta_{iso},C_Q,\eta_Q)$) characteristic to the defect pyrochlore samples (Bi_3NbO_7 and $Sn_2Nb_2O_7$) from these datasets, a previously described numerical inversion procedure has been applied.[60–62] The aim of this procedure is to reconstruct the distribution $P(\delta_{iso},C_Q,\eta_Q)$ numerically on a grid of discrete values of $\delta_{iso}{}^i$, $C_Q{}^j$, $\eta_Q{}^k$ without analytical expressions used to model the distributions nor any assumptions made about the number of sites involved. Taking into account all of the experimental effects from the pulse sequence (such as pulse width and finite spinning rate) allows this procedure to become quantitative.[63] This computational task is referred to as an ill-posed problem, and numerical techniques such as a Tikhonov regularisation have to be invoked.[64] The standard procedure central to this method requires that the algorithm minimises the functional given in [Eq. (8)] in which α is the regularisation coefficient that controls the amount of smoothness induced by the regularising term $||D^{(1)}\Pi||$, which aims to minimise the first-order derivative of the Π distribution.

$$\boldsymbol{L}(\Pi) = \frac{1}{2}\chi^2 + \alpha\|D^{(1)}\Pi\| \tag{8}$$

The regularisation coefficient α has been chosen manually so as to obtain a satisfactory distribution that exhibits a good agreement with the experimental data, and [Eq. (8)] is solved by using a non-negativeness constraint on Π. Because the 2D experimental data for disordered or amorphous materials are relatively featureless, it is difficult to extract a 3D distribution from 2D data. For this reason, the asymmetry parameter η_Q was chosen to remain constant to facilitate extraction of the distributions in δ_{iso} and C_Q only, and it was consistently found that the resulting distribution $P(\delta_{iso},C_Q,\eta_Q)$ is quite insensitive to the choice of η_Q.

In contrast, for the simulation of 1D ^{93}Nb MAS NMR spectra from disordered systems, previously described analytical expressions for the ^{93}Nb NMR parameter distributions have been incorporated into a home-developed software simulation package.[65] The total distribution is given by the product shown in [Eq. (9)] in which the Gaussian isotropic (or Czjzek) model $P(C_Q,\eta_Q)$ was used for the EFG interaction parameters,[66,67] and a normal (or Gaussian) distribution model $G(\delta_{iso})$ was used for the isotropic chemical shift.

$$\pi(\delta_{iso},C_Q,\eta_Q) = P(C_Q,\eta_Q) \times G(\delta_{iso}) \tag{9}$$

An optimal constraint of these B_0 field-dependent parameters was achieved by interactive analysis of these line shapes at the various spectrometer fields outlined above. The B_0 field-dependent variation of the centre-of-gravity shift (δ_{cg}) of featureless 1D ^{93}Nb MAS NMR resonances is also used to measure NMR interaction parameters from disordered systems. From well-established quantum mechanical treatments of the MAS NMR properties of quadrupolar nuclei, the apparent or centre-of-gravity shift of a ($-1/2 \leftrightarrow +1/2$) central transition resonance at any particular B_0 field is given by the sum shown in [Eq. (10)][68] in which the isotropic shift δ_{iso} is augmented by a field- and spin-number-dependent second-order quadrupolar shift term $\delta_{Q,iso}{}^{(2)}(I,m)$, which can be expressed as shown in [Eq. (11)].[68,69]

$$\delta_{cg} = \delta_{iso} + \delta_{Q,iso}{}^{(2)}(I,m) \tag{10}$$

$$\delta_{Q,iso}{}^{(2)}(I,m) = (3C_Q{}^2/(40\nu_o{}^2I^2(2I-1)^2))[I(I+1)-9m(m-1)-3](1+\eta_Q{}^2/3) \tag{11}$$

Hence, if the variation in δ_{cg} is monitored as a function of B_0 (i.e., with δ_{cg} being plotted against $1/\nu_o{}^2$), then by graphical methods the isotropic shift δ_{iso} and the quadrupolar interaction constant P_Q are obtained from the y intercept and slope of this data, respectively. The quadrupolar interaction constant P_Q is given by [Eq. (12)][70–72] in which the quadrupole coupling constant C_Q and asymmetry parameter η_Q are degenerate within this parameter.

$$P_Q = C_Q\sqrt{(1+\eta_Q{}^2/3)} \tag{12}$$

DFT and SIMPSON methodology: CS and EFG tensors were calculated from published structures by using the DFT-based NMR-CASTEP,[73–75] WIEN2k[76] and Gaussian 03[77] codes. The NMR-CASTEP and WIEN2k programs were developed for the calculation of physical properties from periodic structures, whereas Gaussian 03 focuses on atomic/molecular orbital structure in more isolated molecular fragments, clusters and small molecules. WIEN2k is an all-electron calculation that relies on the separation of each periodic structure into two regions consisting of atomic spheres and interstitial regions delineated by the muffin-tin radius (R_{MT}). This method is able to generate EFG tensors for any element, but it does not accommodate virtual excited valence states and thus cannot be employed for the calculation of CS parameters. NMR-CASTEP is enabled by the gauge included projector augmented wave (GIPAW) formalism, and is subtly different because it utilises the core electrons from a free-atom calculation to generate a frozen core, with interactions between the core and valence electrons being described by using element-specific pseudopotentials. Only the valence electrons are allowed to vary during calculation, with the valence-electron wave functions and their corresponding charge density being described by using a plane-wave basis set. Hence, it is essentially a valence calculation in which virtual excited-state electronic structure is invoked, thus permitting the calculation of CS parameters. Pre-release Nb, La, Na and Mg, and default O on-the-fly (OTF) pseudopotentials were provided by the Accelrys company for calculating ^{93}Nb NMR interaction parameters with other elements being described by ultra-soft pseudopotentials. Gaussian 03 restricted Hartree–Fock (RHF) and hybrid density functional theory (B3LYP) methods were implemented,[78,79] with all-electron basis sets (either 16s10p7d(5s2) or 16s10p7d(5s1)) or the DZVP basis set being used for Nb atoms,[80] and the 6-311++G** basis set was used for all lighter atoms.

WIEN2k calculations utilised the GGA (PBE) exchange correlation potential with standard settings plus those detailed here and in Table 1. Muffin-tin radii (R_{MT}) for oxygen sites were in the range $1.5a_0$ to $1.6a_0$. The separation energy between core and valence states was chosen for each structure to treat any states above -10 Ry as valence states. Calculations were made with different numbers of k points for two values of the ratio $R_{MT}k_{max}$ (7 and 8) to test that the NMR parameters had converged. The requested number of points was set as 10, 50 and 200 for each structure, with additional points being specified when necessary. $G_{max}=14.0$ was used in all cases. NMR-CASTEP was run through the Accelrys Materials Studio Modelling 4.2 interface by using the GGA

Table 1. The reported niobate space group, actual cells used in calculation and number of k points implemented in the NMR-CASTEP and WIEN2k calculations.

Niobate system	ICSD code	Space group	Cell used	CASTEP		WIEN2k[a]	
				k	k_{CSA}	k	$^{Nb}R_{MT}/a_0$
$YNbO_4$	20335	$C2/c$	primitive	$5\times5\times7$	44	$5\times5\times6$[b]	1.9000
$LaNbO_4$	81616	$I2/a$	primitive	$5\times5\times6$	45	$5\times5\times6$[b]	1.9300
$CaNb_2O_6$	15208	$Pbcn$	no change	$2\times4\times5$	3	$2\times7\times8$	1.8500
$MgNb_2O_6$	85008	$Pbcn$	no change	$2\times4\times5$	3	$3\times7\times8$	1.9200
La_3NbO_7	79481	$Pnma$	no change	$3\times2\times3$	2	$6\times4\times6$	2.1358
$Mg_4Nb_2O_9$	91748	$P\bar{3}c1$	no change	$6\times6\times2$	11	$8\times8\times2$	1.9700
$SnNb_2O_6$	202827	$C2/c$	primitive	$5\times5\times4$	15	$6\times6\times5$[b]	1.8900
$BiNbO_4$	74338	$Pnna$	no change	$4\times2\times5$	3	$7\times3\times8$	1.8990
$Cd_2Nb_2O_7$	75601	$Fd\bar{3}m$	primitive	$4\times4\times4$	15	$7\times7\times7$[b]	2.0600
$CsBiNb_2O_7$	96510	$P2_1am$	$Pmc2_1$	$2\times5\times5$	9	$3\times7\times7$	1.8163
$LiNbO_3$	94493	$R3ch$	$R3c$	$6\times6\times6$	28	$7\times7\times7$[b]	2.0014
$NaNbO_3$	23239	$Pbcm$	no change	$3\times5\times4$	3	$11\times11\times3$	1.9324
	74642	$P2_1ma$	no change	$4\times3\times5$	6	–	–
	97669	$Pbma$	no change	$3\times5\times4$	3	–	–
$KNbO_3$	9533	$Amm2$	primitive	$6\times6\times6$	18	$9\times9\times10$[b]	1.9400

[a] Convergence was tested by using $R_{MT}k_{max}$ ratios up to 8.0. [b] Symmetries were converted to $P1$ for use with WIEN2k.

(PBE) functional. The unit cell and symmetry recommended by the interface was accepted (see 'cell used' in Table 1), and these were maintained for the corresponding WIEN2k calculations. The number of unfilled bands was set to 24 for all structures, except in the $Mg_4Nb_2O_9$ case for which 44 were used. Other parameters were set by using the coarse, medium, fine and ultra-fine settings of the interface, and these were used to test the convergence of the NMR parameters. For an ultra-fine setting defined by an energy cut off = 610 eV and SCF tolerance = 5×10^{-7} eV/atom, the associated numbers of k points used for each structure are given in Table 1. The WIEN2k calculations, by default, treated the core electrons in a fully relativistic manner and subjected the valence states to a scalar relativistic treatment, the NMR-CASTEP calculations treated the core electrons only in a scalar relativistic manner, whereas the Gaussian 03 calculation is completely non-relativistic.

Structural .cif files were taken from the Inorganic Crystal Structure Database (ICSD) with the relevant collection codes provided in Table 1. Some primitive unit cells were reduced to $P1$ symmetry for WIEN2k calculations owing to problems with its interpretation of certain space groups. Structural optimisations were performed for most of the niobate compounds by using NMR-CASTEP. However, the resulting ^{93}Nb NMR interaction parameters showed significantly inferior agreement with experimental values in almost all cases. All NMR-CASTEP and WIEN2k calculations were performed by using dual-2.0 GHz/dual core Hewlett Packard xw9300 AMD Opteron workstations running Red Hat Linux 9.0 and required no more than 4 GB and 1.2 GB of RAM, respectively. Gaussian 03 calculations were performed on dual-2.8 GHz Xenon Dell Precision 650 or dual-3.6 GHz Xenon Dell Precision 670n workstations running Red Hat Linux 9.0, and selected calculations were directed to larger cluster facilities under the SHARCNET computer network.

SIMPSON simulations[81] of some MAS NMR spectra were performed on Pentium-4-class computers with the zcw28656 crystallite file and 19 gamma angles, with the calculated FID inclusive of all quadrupolar satellites. A solid-echo $\pi/2$–τ–$\pi/2$–τ–(acquire) sequence was implemented with 5 μs pulses (B_1 = 10 kHz) to limit the excited spectral width of the calculated quadrupolar satellites. Each simulation took several days to complete and the resultant FID was processed by using the Varian-Chemagnetics Spinsight software package.

Results and Discussion

^{93}Nb broadline & MAS NMR: The ^{93}Nb static (broadline) central transition data and fast MAS data for the suite of niobate compounds studied are shown in Figures 2–4. Figure 2 shows the very broad ^{93}Nb spectra for four-coordinate orthoniobate systems. These form an uncommon subset of coordination environments in Nb^V-oxide chemistry that are usually dominated by higher coordination numbers such as 6, 7 and 8. These rare-earth metal containing systems are

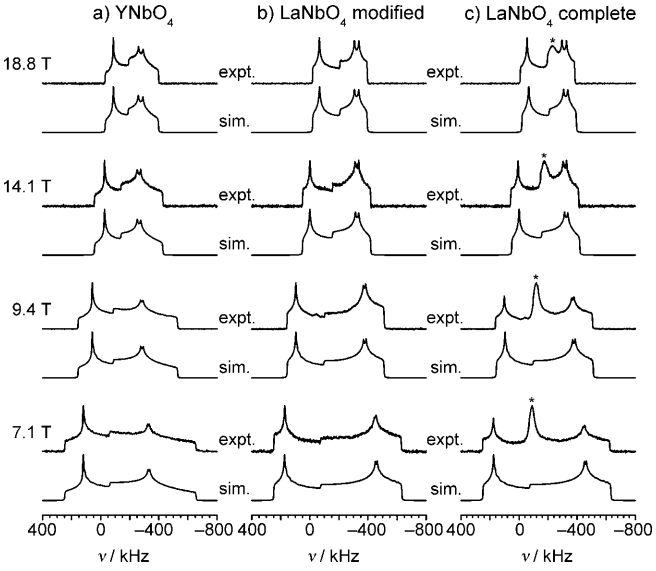

Figure 2. Variable B_0 field VOCS arrayed ^{93}Nb ($-1/2\leftrightarrow+1/2$) central transition spectra for a) $YNbO_4$, b) $LaNbO_4$ (modified) and c)$LaNbO_4$ (complete), which exhibit C_Q values of >80 MHz. The modified $LaNbO_4$ data is generated by subtracting the narrow resonance associated with ionic conduction/oxygen defects away from each complete $LaNbO_4$ line shape. Sim. = simulated, expt. = experimental.

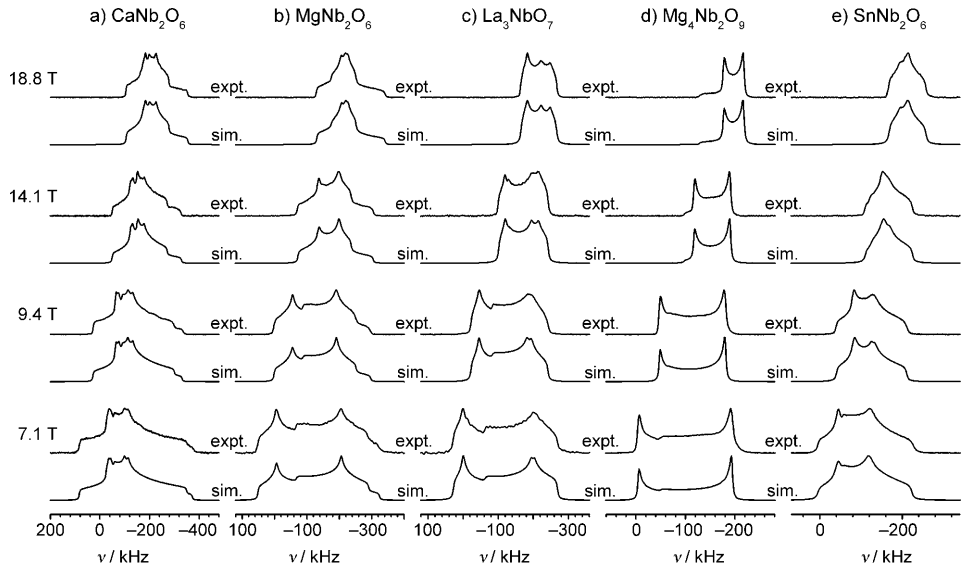

Figure 3. Variable B_0 field VOCS arrayed ^{93}Nb ($-1/2 \leftrightarrow +1/2$) central transition spectra for a) $CaNb_2O_6$, b) $MgNb_2O_6$, c) La_3NbO_7, d) $Mg_4Nb_2O_9$ and e) $SnNb_2O_6$, which exhibit C_Q values in the 35–55 MHz range. Sim. = simulated, expt. = experimental.

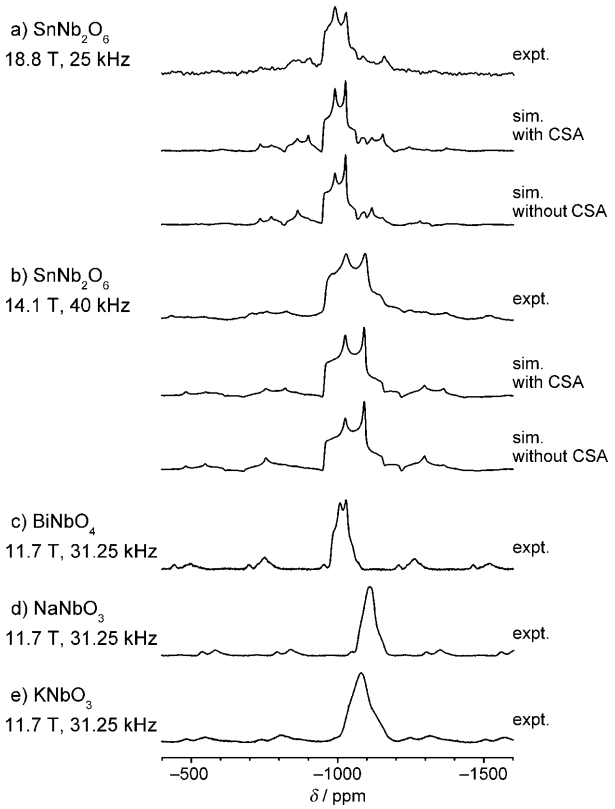

Figure 4. Fast MAS NMR data acquired for a) $SnNb_2O_6$ (18.8 T, ν_r = 25 kHz) with associated SIMPSON simulations, b) $SnNb_2O_6$ (14.1 T, ν_r = 40 kHz) with associated SIMPSON simulations, c) $BiNbO_4$ (11.7 T, ν_r = 31.25 kHz), d) $NaNbO_3$ (11.7 T, ν_r = 31.25 kHz) and e) $KNbO_3$ (11.7 T, ν_r = 31.25 kHz). Sim. = simulated, expt. = experimental.

represented by monoclinic $YNbO_4$ and $LaNbO_4$, which adopt the fergusonite structures and crystallise into the $C12/c1$ and $I12/a1$ space groups, respectively. They are sometimes considered as pseudo six-coordinate environments because they represent discrete tetrahedra (typical Nb–O bond lengths of ~1.86 Å) within a NbO_4 chain, with two additional longer Nb–O bonds (2.4–2.5 Å) extending to adjacent NbO_4 chains.[42,43] The point symmetry of each four-coordinate environment is distorted thus promoting the very broad ^{93}Nb resonances observed in Figure 2a and b, and the concomitant large C_Q values of >80 MHz as reported in Table 2. As such, the accurate measurement of these data relies profoundly on the VOCS method for the reconstruction of undistorted central transition spectra, as illustrated in Figure 1. Some large discrepancies exist between the data presented here for these materials and what has been previously reported in the literature.[28] In particular, the C_Q values reported in this study (see Table 2) are considerably larger in magnitude. This is most evident for $LaNbO_4$ in which C_Q is 16 MHz greater than previously reported values; this is attributed to the previous neglect of a considerable CSA contribution to the ^{93}Nb line width ($\Omega >$ 400 ppm). This underestimation of C_Q also introduced a significant error in δ_{iso}, which actually occurs ~200 ppm more shielded (upfield) from previously reported values. This original ^{93}Nb data has been recently updated and a CSA contribution has been introduced, and although the discrepancy is reduced the magnitude of the CSA ($\Delta\delta$) contribution still appears to be underestimated by ~160 ppm.[29] A similar yet reduced effect is observed for $YNbO_4$ in which the $\Delta\delta$ measurements reported in this work are greater by ~70 ppm.[29]

It has been reported that this class of materials demonstrates mixed fast protonic, native ionic and electronic conduction properties depending on the synthesis and measurement conditions, with doped $LaNbO_4$ exhibiting the highest propensity for this type of behaviour.[82] From Figure 2c it can be observed that at each B_0 field a narrower featureless resonance is located on top of the broad second-order quadrupole/CSA dominated line shape, which is presumably linked with some partial disorder and oxygen defects associated with these physical properties. This resonance has been subtracted from the ^{93}Nb central transition spectrum at each B_0 field to enable the broader resonance from the ordered bulk material to be accurately simulated (see Figure 2b and Figure 2c).

Table 2. Experimentally measured and WIEN2k/NMR-CASTEP DFT calculated ^{93}Nb NMR interaction parameters for various niobate systems.

Niobate system	Coord. number	δ_{iso} [ppm] (±5)	C_Q[a] [MHz] (±0.03)	η_Q[a] (±0.003)	Ω[b] [ppm] (±5)	κ[b] (±0.003)	$\Delta\delta$[c] [ppm] (±5)	η_δ[c] (±0.003)	δ_{11} [ppm] (±5)	δ_{22} [ppm] (±5)	δ_{33} [ppm] (±5)	α [deg] (±2)	β [deg] (±2)	γ [deg] (±2)	WIEN2k C_Q	WIEN2k η_Q	NMR-CASTEP δ_{iso}	NMR-CASTEP C_Q	NMR-CASTEP η_Q	Ω[b]	κ[b]
$YNbO_4$	4	−840	82.23	0.381	307	−0.498	−269	0.430	−712	−789	−1019	−1	17	95	82.5	0.41	−915	76.6	0.41	345	−0.414
$LaNbO_4$	4	−853	86.55	0.186	423	−0.369	−357	0.559	−668	−801	−1091	−13	11	95	100.9	0.12	−816	95.9	0.11	422	−0.288
$CaNb_2O_6$	6	−975	50.40	0.787	526	−0.314	−437	0.619	−740	−920	−1266	43	143	−10	−43.1	0.79	−1003	−41.7	0.78	440	−0.601
$MgNb_2O_6$	6	−1020	53.81	0.248	584	−0.544	−518	0.386	−781	−914	−1365	26	63	−15	−54.3	0.30	−1012	−50.7	0.27	541	−0.661
La_3NbO_7	6	−998	50.87	0.212	249	+0.554	+222	0.372	−1099	−1044	−850	50	19	85	−46.1	0.00	−936	−45.6	0.05	259	+0.953
$Mg_4Nb_2O_9$	6	−921	45.55	0.000	389	+1.000	+389	0.000	−1051	−1051	−662	0	0	0	−44.0	0.00	−878	−43.3	0.00	386	+1.000
$SnNb_2O_6$	6	−1014	40.06	0.477	291	+0.206	+233	0.748	−1150	−1034	−859	90	157	90	−35.9	0.59	−1000	−32.8	0.55	264	+0.280
$BiNbO_4$	6	−969	20.83	0.534	261	−0.494	−228	0.434	−860	−926	−1121	14	18	83	23.6	0.50	−979	22.5	0.49	217	−0.636
$Cd_2Nb_2O_7$	6	−988	24.79	0.000	9	−1.000	−9	0.000	−985	−985	−994	0	0	0	−29.7	0.00	−918	−29.1	0.00	3	−0.991
$CsBiNb_2O_7$	6	−936	24.06	0.473	756	−0.806	−720	0.152	−660	−733	−1416	17	24	117	−24.4	0.58	−947	−24.5	0.56	636	−0.887
$LiNbO_3$	6	−988	22.25	0.000	172	+1.000	+172	0.000	−1045	−1045	−873	0	0	0	−24.4	0.00	−958	−22.3	0.00	170	+1.000
$NaNbO_3$[d]	6	−1064	19.96	0.785	116	−0.543	−104	0.379	−1017	−1043	−1133	11	99	95	−22.7	0.64	−1017	−20.8	0.22	88	−0.314
$NaNbO_3$[e]	6	–	–	–	–	–	–	–	–	–	–	–	–	–	–	–	−944	−15.1	0.28	97	−0.670
$NaNbO_3$[f]	6	–	–	–	–	–	–	–	–	–	–	–	–	–	–	–	−978	−57.1	0.57	131	−0.614
$KNbO_3$	6	−1019	22.99	0.822	117	−0.641	−107	0.296	−973	−994	−1090	23	94	81	−21.6	0.95	−965	−19.8	0.97	107	−0.637
Bi_3NbO_7[g]	6	ca. −961	ca. 22.0	–	–	–	–	–	–	–	–	–	–	–	–	–	–	–	–	–	–
$Sn_2Nb_2O_7$[g]	6	ca. −1019	ca. 18.7	–	–	–	–	–	–	–	–	–	–	–	–	–	–	–	–	–	–

[a] EFG tensor conventions: $|V_{33}| \geq |V_{22}| \geq |V_{11}|$, $C_Q = e^2qQ/h = eQV_{33}/h$, $\eta_Q = (V_{11} - V_{22})/V_{33} (1 \geq \eta_Q \geq 0)$. [b] Herzfeld–Berger shift convention: $\delta_{11} \geq \delta_{22} \geq \delta_{33}$ (tensorial representation not shown above), $\delta_{iso} = (\delta_{11} + \delta_{22} + \delta_{33})/3$, $\Omega = (\delta_{11} - \delta_{33})$, $\kappa = 3(\delta_{22} - \delta_{iso})/(\delta_{11} - \delta_{33})$ $(1 \geq \kappa \geq -1)$. [c] Haeberlen shift convention: $|\delta_{33} - \delta_{iso}| \geq |\delta_{11} - \delta_{iso}| \geq |\delta_{22} - \delta_{iso}|$ (tensorial representation shown above), $\delta_{iso} = (\delta_{11} + \delta_{22} + \delta_{33})/3$, $\Delta\delta = \delta_{33} - 1/2(\delta_{11} + \delta_{22}) = 3/2(\delta_{33} - \delta_{iso})$, $\eta_\delta = (\delta_{22} - \delta_{11})/(\delta_{33} - \delta_{iso})$ $(1 \geq \eta_\delta \geq 0)$. [d] ICSD 23239, *Pbcn*, 1969. [e] ICSD 74642, *P2ma*, 1993. [f] ICSD 97669, *Pbma*, 2003. [g] Average of values derived from different experimental methods, see Table 3.

Figure 3 shows the variable B_0 field ^{93}Nb central transition data for a series of niobate materials possessing six-coordinate Nb^V environments and exhibiting C_Q values in the range of ~35–55 MHz. In a similar fashion to the data presented in Figure 2, these line shapes are also heavily reliant on the VOCS method for the acquisition of undistorted central transition data, as exemplified in Figure 1b and c. $CaNb_2O_6$, $MgNb_2O_6$ and La_3NbO_7 are the first systems represented in this series (see Figure 3a–c) and they all possess orthorhombic symmetry; the first two crystallise into the *Pbcn* space group with the columbite structure[44,83] and the latter crystallises into the *Pnma* space group with the fluorite structure.[84] In the columbite cases, the octahedra are distorted and one Nb–O bond is noticeably longer than its counterparts thereby allowing this Nb^V coordination to be also described as pseudo five coordinate. They both exhibit similar C_Q values of >50 MHz (50.40 MHz for $CaNb_2O_6$, 53.81 MHz for $MgNb_2O_6$), and both exhibit a substantial CSS contribution to the ^{93}Nb line width ($\Omega > 520$ ppm for each). However, significantly different isotropic chemical shifts have been measured for $CaNb_2O_6$ (δ_{iso} −(975±5) ppm) and $MgNb_2O_6$ (δ_{iso} −(1020±5) ppm), suggesting that the ^{93}Nb chemical shift is sensitive to the ionic radius and proximity to the divalent cations in this structure, which are not within the immediate Nb–O coordination spheres. La_3NbO_7 exhibits a C_Q value of similar magnitude (50.87 MHz), but a much reduced CSS contribution ($\Omega = 249$ ppm) in comparison with its above-mentioned orthorhombic counterparts. The immediate oxo coordination environment of each Nb position in La_3NbO_7 is much less distorted in comparison with the columbite structures, further implying that electronic influences from outside this immediate sphere are highly significant. The broadline ^{93}Nb NMR data shown in Figure 3d are for the higher-order magnesium niobate $Mg_4Nb_2O_9$, which possesses hexagonal symmetry and crystallises into the $P\bar{3}c1$ space group with the corundum structure.[85,86] This niobate structure is one of the few that affords the Nb position three-fold rotational point symmetry as evidenced by the axially symmetric EFG and CS tensors described in Table 2. The measured C_Q value of 45.55 MHz is almost as large as that reported above for the orthorhombic cases. However, similar to the La_3NbO_7 case, the absolute variation in Nb–O bond distances is not as pronounced, consequently reinforcing the notion that the immediate point symmetry of each Nb position in these niobates is not a direct determinant of the ^{93}Nb NMR interaction parameters. A further salient example of this phenomenon is the $Mg_4Nb_2O_9$ isotropic chemical shift observed at δ_{iso} −(921±5) ppm, which represents the highest of the six-coordinate niobate shifts studied here. This disparate value is

clearly outside the proposed chemical shift range for six-coordinate Nb sublattices of variable ionic character proposed by Lapina et al.[28,29]

The monoclinic $SnNb_2O_6$ system with the foordite structure (space group $C12/c1$) has been previously studied by a number of authors who have all neglected the presence of a CSS/CSA contribution to their ^{93}Nb powder line-shape data.[28–30] Variable B_0 field behaviour as shown in Figure 3e clearly demonstrates that a non-negligible CSS/CSA significantly contributes to these line widths. For systems like $SnNb_2O_6$ exhibiting a mid-range C_Q of ~40 MHz and that are characterised by smooth, less-defined singularities in the static data, fast ^{93}Nb MAS techniques can be of assistance in identifying the magnitude and asymmetry of the EFG tensor. However, it is questionable whether this MAS data can be used to deconvolute both quadrupolar and chemical shift contributions accurately. This is demonstrated by the high-field fast MAS data acquired for $SnNb_2O_6$ at 18.8 (ν_r= 25 kHz) and 14.1 T (ν_r=40 kHz) as shown in Figure 4a and b, respectively, with their associated SIMPSON simulations. At these fields the MAS-averaged quadrupolar line shape for the central transition is evident and readily measured, yet further analysis/simulation of the second-order side bands in attempting to elucidate a CSA component is prone to considerable error. From Figure 4a and b, the comparison of the SIMPSON simulations including and excluding a CSA contribution does not sufficiently differ within the second-order side bands to discern accurate solutions for δ_{iso}, Ω, κ (or $\Delta\delta$, η_δ), α, β and γ. A more rigorous approach is to deploy the quadrupole parameters obtained under high-field/fast MAS conditions directly into the simulation and deconvolution of the static NMR data, which displays far greater spectral variation with B_0, as undertaken in Figure 3e.

Figure 5 shows ^{93}Nb static data for a series of niobate materials that exhibit C_Q values of $<$30 MHz. These much narrower line shapes usually do not require the VOCS method of subspectral addition for the acquisition of undistorted central transition data, and their line widths also make them amenable to study by MAS techniques. The variable-field data for orthorhombic $BiNbO_4$ (space group *Pnna*) in Figure 5a reveals large spectral changes over the B_0 range spanning 4.7–18.8 T, predominantly owing to the quadrupole and chemical shift contributions to the line width being of similar magnitudes. Close inspection of this data shows that as B_0 is increased the central transition spectrum continues to narrow up to the 9.4–14.1 T region, and then starts to broaden again as the CSS/CSA contribution assumes dominance. The MAS data of Figure 4c, and the 3QMAS measurements and subsequent data inversion (see Figure 6a and b) for $BiNbO_4$ yields values of δ_{iso}−(975±3) ppm and C_Q= (21.0±0.2) MHz (for a fixed value of η_Q=0.5), which are in good agreement with the static results presented in Table 2. However, this data is only diagnostic of the quadrupole interaction because MAS eliminates the CSA component, and it can be used in a similar fashion to the $SnNb_2O_6$ case described above. The EFG parameters elucidated under MAS conditions can, therefore, present a reliable basis for the complete simulation of the corresponding static data thus supporting accurate measurement of the CS parameters Ω, κ (or $\Delta\delta$, η_δ) and the Euler angles α, β and γ.

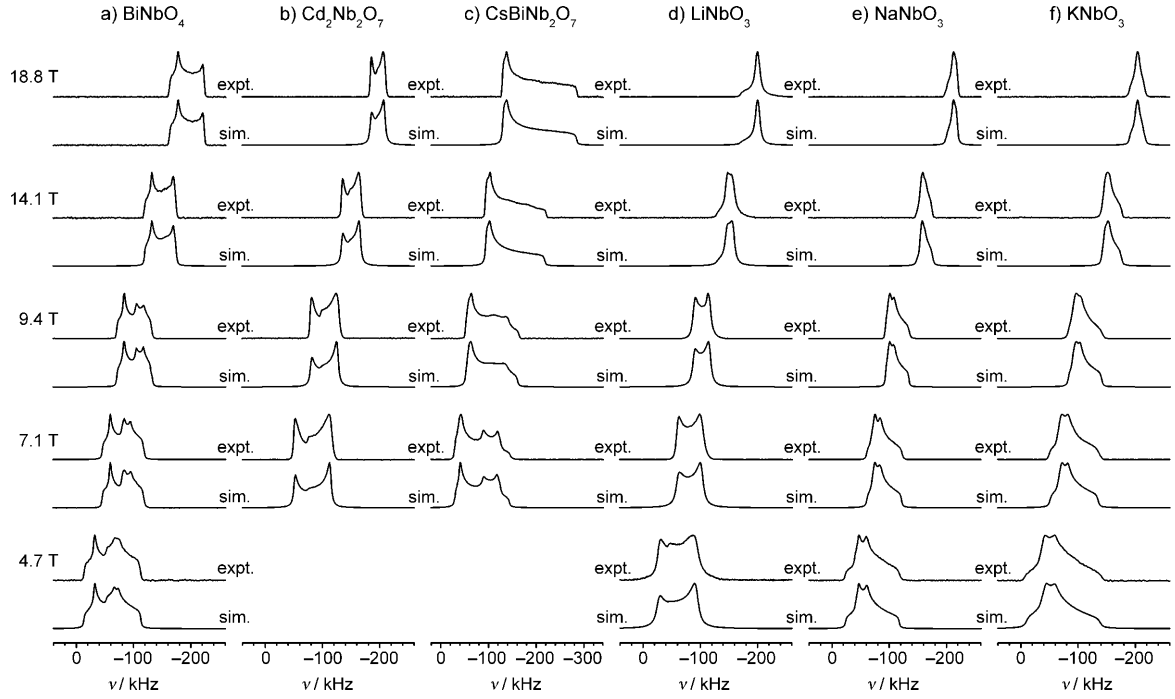

Figure 5. Variable B_0 field single-offset ^{93}Nb ($-1/2\leftrightarrow+1/2$) central transition spectra for a) $BiNbO_4$, b) $Cd_2Nb_2O_7$, c) $CsBiNb_2O_7$, d) $LiNbO_3$, e) $NaNbO_3$ and f) $KNbO_3$, which exhibit C_Q values in the $<$30 MHz range. Sim.=simulated, expt.=experimental.

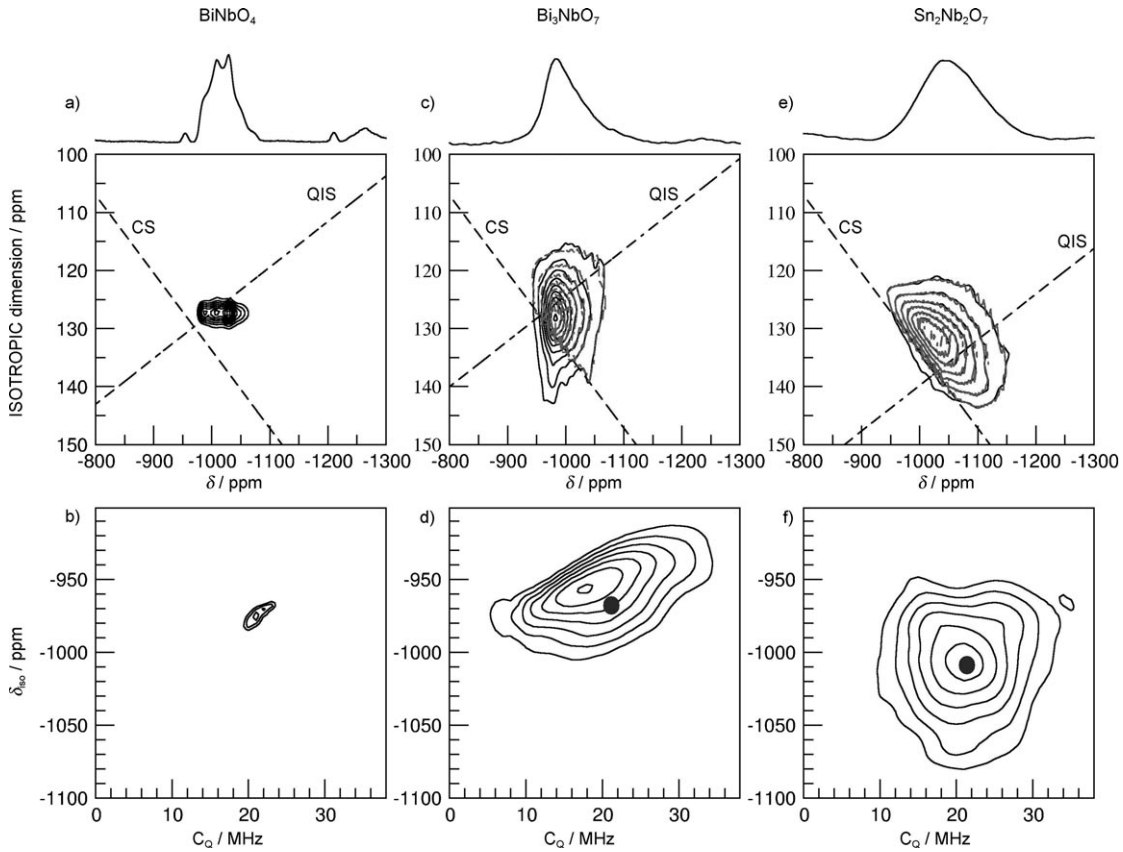

Figure 6. a) $BiNbO_4$ 3QMAS data, b) $BiNbO_4$ inversion data, c) Bi_3NbO_7 3QMAS data, d) Bi_3NbO_7 inversion data, e) $Sn_2Nb_2O_7$ 3QMAS data and f) $Sn_2Nb_2O_7$ inversion data, all acquired at 11.7 T with the amplitude-modulated Z-filter p_1–t_1(3Q evolution)–p_2–τ–p_3–t_2(acquire) experiment.

The next two data sets in Figure 5 for $Cd_2Nb_2O_7$ (see Figure 5b) and $CsBiNb_2O_7$ (see Figure 5c) represent two very unusual cases in the measurement of ^{93}Nb NMR interaction parameters in niobate systems. $Cd_2Nb_2O_7$ is a classic pyroniobate with a cubic defect-pyrochlore structure, which crystallises into the $Fd\bar{3}m$ space group. The well-defined powder line-shape data of Figure 5b suggests that the O defects are only a minor percentage of the total O speciation in this structure. Its isotropic chemical shift of $\delta_{iso}-(987\pm5)$ ppm conforms to the proposed shift range of Lapina et al. for cubic niobate systems.[28,29] However, it displays a vanishingly small CSS ($\Omega < 10$ ppm) in conjunction with a moderately sized C_Q value of ~25 MHz and an environment that dictates rotational point symmetry (see the axially symmetric NMR interaction tensors reported in Table 2). In contrast, the layered perovskite $CsBiNb_2O_7$ (space group $P2_1am$) is observed at a high shift of $\delta_{iso}-(936\pm5)$ ppm, which disagrees with the above-mentioned proposed shift ranges, and although it possesses a quadrupolar interaction similar in magnitude to $Cd_2Nb_2O_7$ (C_Q ~24 MHz) it also exhibits an enormous CSS contribution. The span of $\Omega = 756$ ppm is clearly the largest reported for any niobate system, but is smaller in magnitude than the largest reported ^{93}Nb CSS values for the oxyfluoroniobates $[Cd(py)_4(NbOF_5)]$ (py = pyridine) and $[pyH]_2[Cd(py)_4(NbOF_5)_2]$ in which $\Omega = (1000\pm20)$ and (1100 ± 20) ppm, respectively.[32] From Figure 5c it can be observed that the CSS is the dominant contribution to these ^{93}Nb static data acquired over the 7.1–18.8 T B_0 range as the line widths increase monotonically with increasing B_0 throughout this series. These observations for $CsBiNb_2O_7$ are a consequence of the NbO_6 octahedra possessing a Cs^I species of very large ionic radius in the next-nearest-neighbour interlayer positions,[87] in contrast to the differing F and O ionic and electron-donation properties characterising the immediate $NbOF_5$ coordination environment in the oxyfluoroniobates.[32] The remaining data in Figure 5 pertains to the alkali niobate perovskites $LiNbO_3$, $NaNbO_3$ and $KNbO_3$ shown in Figure 5d–f, respectively. Rhombohedral $LiNbO_3$ (space group $R3ch$) has been thoroughly investigated in many studies,[12,28,29,50,88–92] however, none of this work has reported a distinct CSS/CSA contribution within any of the ^{93}Nb NMR data that has been presented to date. From Figure 5d and Table 2 it can be observed that a sizeable CSS of $\Omega = 172$ ppm has been measured in this work. Orthorhombic $NaNbO_3$ (space group $Pbcm$) possesses a structure that has been subjected to considerable controversy and discussion over many years,[93–99] although some of the early structural determinations are still very prominent in this debate.[93] In contrast, there is little dispute concerning the structure of orthorhombic $KNbO_3$ (space group $Amm2$).[100] $NaNbO_3$ and $KNbO_3$ exhibit similar ^{93}Nb static spectra from which small but clearly

defined CSS/CSA contributions can be deconvoluted. Although the smaller C_Q values (~20 MHz) characterising these systems should be responsive to the introduction of MAS techniques, as illustrated in Figure 4d and e the MAS-averaged central transition spectral features in these materials tend to be smoothed and of limited use when accurate values of δ_{iso}, C_Q and η_Q are being sought. Upon initial measurement of moderately accurate δ_{iso}, C_Q and η_Q values from this MAS data, recourse to the more highly B_0 dependent static data of Figure 5e and f for elucidation of all the ^{93}Nb NMR interaction parameters is a more appropriate option.

The last entries in Table 2 refer to Bi_3NbO_7 and $Sn_2Nb_2O_7$ cubic defect-pyrochlore systems. In contrast to $Cd_2Nb_2O_7$, the latter Bi_3NbO_7 (space group $Fm\bar{3}m$) and $Sn_2Nb_2O_7$ (space group $Fd\bar{3}m$) systems are characterised by significant degrees of partial occupancy on the oxygen and metal positions, thus subjecting the Nb site to substantial structural disorder in its immediate and next-nearest-neighbour environments.[30,101] This is clearly evident in the ^{93}Nb 3QMAS data of Figure 6; 3QMAS data for a structurally ordered material such as $BiNbO_4$ produces tightly defined contours and well-defined δ_{iso}/C_Q results from the inversion process (see Figure 6a) and b), whereas analogous data for Bi_3NbO_7 and $Sn_2Nb_2O_7$ yield broad asymmetric resonances and diffuse contours that are consistent with highly disordered systems (see Figure 6c–f). Less clearly defined solutions for δ_{iso} and C_Q are delineated by the inversion process for these disordered systems. However, the 3QMAS and inverted data both describe characteristic distributions that bear differently upon the EFG and CS parameters of each system. For $Sn_2Nb_2O_7$, a large component of chemical dispersion is depicted by the dominant projections along the CS axis in Figure 6e and along the δ_{iso} axis in Figure 6f. This is corroborated by the ^{93}Nb MAS NMR spectra and simulations shown in Figure 7a, in which the quality of the fit by using a Gaussian isotropic (or Czjzek) distribution model to describe disorder in the quadrupolar interaction at 18.8 T is compromised by a significant contribution from chemical shift dispersion. The data presented in Figures 6 and 7 demonstrate that three different approaches involving 3QMAS and inversion (see Figure 6c–f), direct simulation of variable B_0 MAS data including disorder broadening of quadrupolar line shapes (see Figure 7a) and mapping of the centre-of-gravity shift in the ^{93}Nb MAS resonance with variation in B_0 (see Figure 7b) converge upon values of δ_{iso} and C_Q for these disordered systems with quite reasonable agreement, considering the limitations and approximations of each method. It is evident from Table 3 that the quadrupole parameters for Bi_3NbO_7 and $Sn_2Nb_2O_7$ are similar. However, the δ_{iso} values are very different with (average) δ_{iso} −(961±10) ppm for Bi_3NbO_7 falling within the lower limits of the proposed shift ranges of Lapina et al.,[28,29] whereas $Sn_2Nb_2O_7$ is more shielded with (average) δ_{iso} −(1019±10) ppm occurring marginally outside of these ranges.

This section has clearly described how the CSS/CSA is usually an important and non-negligible contribution to

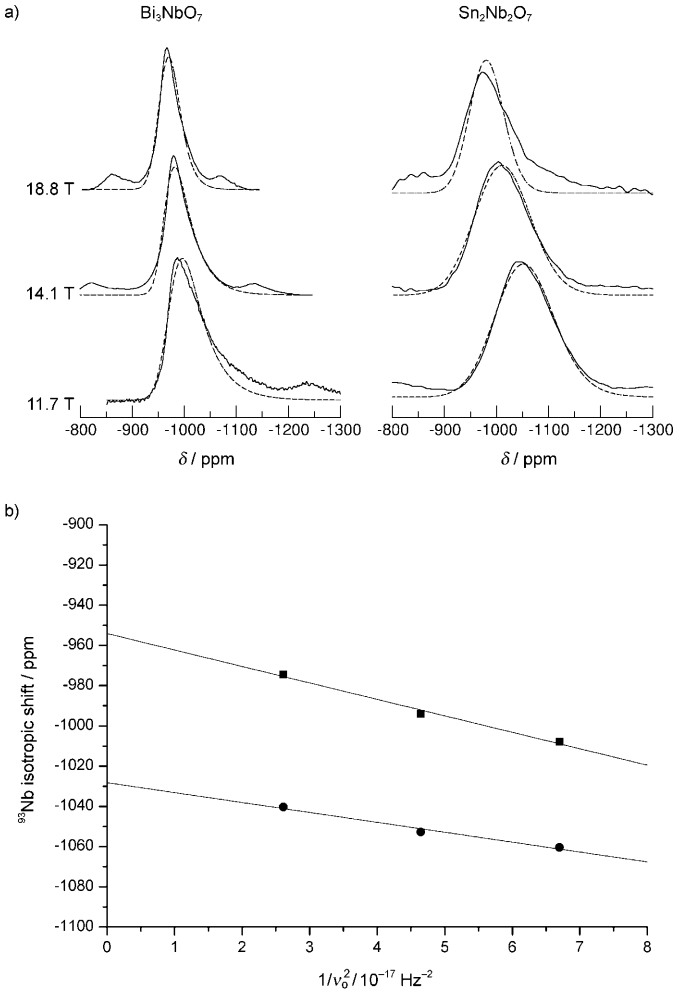

Figure 7. Variable B_0 field studies of the ^{93}Nb MAS NMR resonances for the defect pyrochlores Bi_3NbO_7 and $Sn_2Nb_2O_7$, in which a) the total distributions in the quadrupolar and isotropic chemical shift parameters $\pi(\delta_{iso},C_Q,\eta_Q) = P(C_Q,\eta_Q) \times G(\delta_{iso})$ are described by individual analytical expressions for the distributions in the EFG interaction (Gaussian isotropic (or Czjzek) model, $P(C_Q,\eta_Q)$) and isotropic chemical shift (normal (or Gaussian) distribution model, $G(\delta_{iso})$), respectively, and b) the centre-of-gravity shift (δ_{cg}) of the MAS resonance is monitored as a function of $1/\nu_o^2$ ($Bi\bar{3}NbO_7$ = ■, $Sn_2Nb_2O_7$ = ●).

^{93}Nb NMR line shapes, and that combined static/MAS approaches with variable B_0 studies must be introduced to complement the characteristics of the Nb^V system that is being studied. In addition, when disordered systems are being studied with MAS techniques, the additional complication of chemical shift dispersion often needs to be taken into account.

DFT calculations: The predictive capabilities of DFT calculations for EFG and CS NMR interaction parameters of heavier and transition-metal elements in the solid state has yet to be comprehensively assessed. Although some studies have been reported for ^{93}Nb,[33] $^{47/49}$Ti,[102,103] ^{51}V,[103,104] ^{55}Mn,[105] ^{57}Fe,[106] ^{59}Co,[107,108] ^{77}Se,[109,110] ^{95}Mo,[111] ^{99}Ru,[112] ^{103}Rh,[113,114] ^{125}Te,[109,110] ^{133}La,[115] ^{183}W[116] and ^{195}Pt,[117] the

Table 3. Experimentally elucidated EFG interaction parameters for the disordered defect pyrochlore systems Bi_3NbO_7 and $Sn_2Nb_2O_7$ as determined with a) the 3QMAS/inversion method, b) direct line-shape simulation with quadrupole/quadrupole distribution fitting and c) the variable B_0/graphical approach.

Niobate system	MAS method used							
	3QMAS/inversion		Quadrupole distribution simulation		Variable B_0 field/graphical		Average	
	δ_{iso} ($\pm$10)	C_Q [MHz] ($\pm$1.0)	δ_{iso} ($\pm$10)	P_Q[a] [MHz] ($\pm$1.0)	δ_{iso} ($\pm$10)	P_Q[a] [MHz] ($\pm$1.0)	δ_{iso} ($\pm$10)	C_Q[b] [MHz] ($\pm$1.0)
$BiNbO_4$	−975	21.0	–	–	–	–	–	–
Bi_3NbO_7	−968	21.2	−962	22.4	−954	24.3	−961	22.0
$Sn_2Nb_2O_7$	−1008	21.4	−1021	19.0	−1028	18.8	−1019	18.7

[a] $P_Q = C_Q\sqrt{(1+\eta^2/3)}$. [b] Average of C_Q values after P_Q values were converted to C_Q (see [a] and [Eq. (12)] assuming a mid-range η_Q value of 0.5.

majority of these studies exclusively focus on isotropic chemical shift calculation of complexed metal species in the solution state. Apart from Gaussian 03 calculations on Nb^V half-sandwich cyclopentadienyl complexes,[33] niobate-based material systems (in particular) have not been probed with a combined DFT/^{93}Nb NMR interaction measurement study to test the effectiveness of DFT for this heavier transition-metal element within differing oxo environments. Table 2 contains the all-electron WIEN2k and GIPAW NMR-CASTEP DFT calculated NMR interaction parameters for the suite of niobates included in this study, whereas Figures 8 and 9 graphically summarise the relationships formed between WIEN2k, NMR-CASTEP and the experimentally measured values of δ_{iso}, C_Q, η_Q, Ω and κ (or $\Delta\delta$ and η_δ). Figure 8a and b demonstrate that both WIEN2k and NMR-CASTEP exhibit excellent predictive capabilites for the C_Q parameter over the whole range of values measured in this study (i.e., from ~20 to >80 MHz) with correlation coefficients (R^2) of 0.975 and 0.977, respectively, being obtained. Correlations of similar R^2 value but increased scatter are observed for the η_Q parameter (see Figure 8c and d) because the overall spread reflects an enhanced sensitivity to errors owing to the formal involvement of all three tensorial elements V_{11}, V_{22} and V_{33} defin-

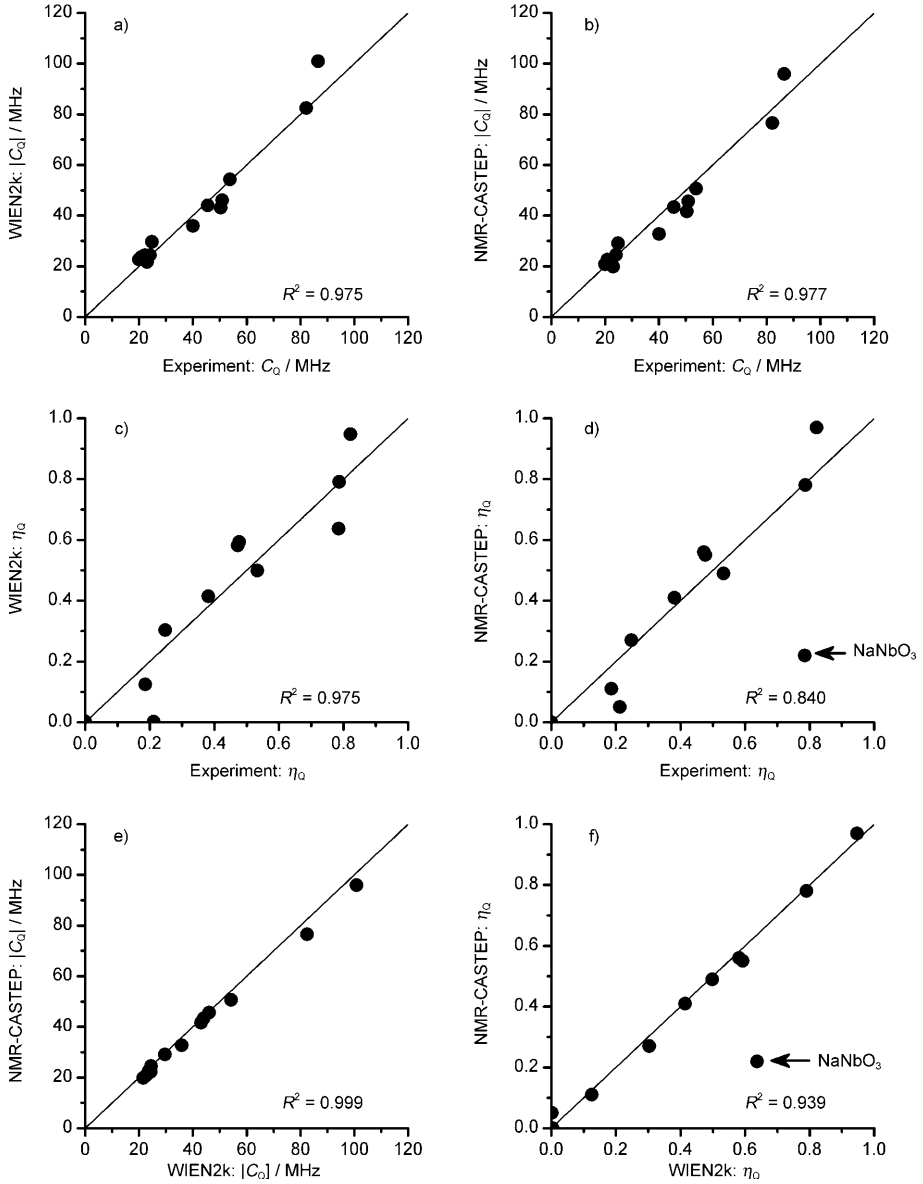

Figure 8. Graphical correlations drawn for the EFG interaction parameters from a) WIEN2k calculated $|C_Q|$/experimentally measured C_Q, b) NMR-CASTEP calculated $|C_Q|$/experimentally measured C_Q, c) WIEN2k calculated η_Q/experimentally measured η_Q, d) NMR-CASTEP calculated η_Q/experimentally measured η_Q, e) NMR-CASTEP calculated $|C_Q|$/WIEN2k calculated $|C_Q|$ and f) NMR-CASTEP calculated η_Q/WIEN2k calculated η_Q, for the suite of four- and six-coordinate niobate systems studied in this work.

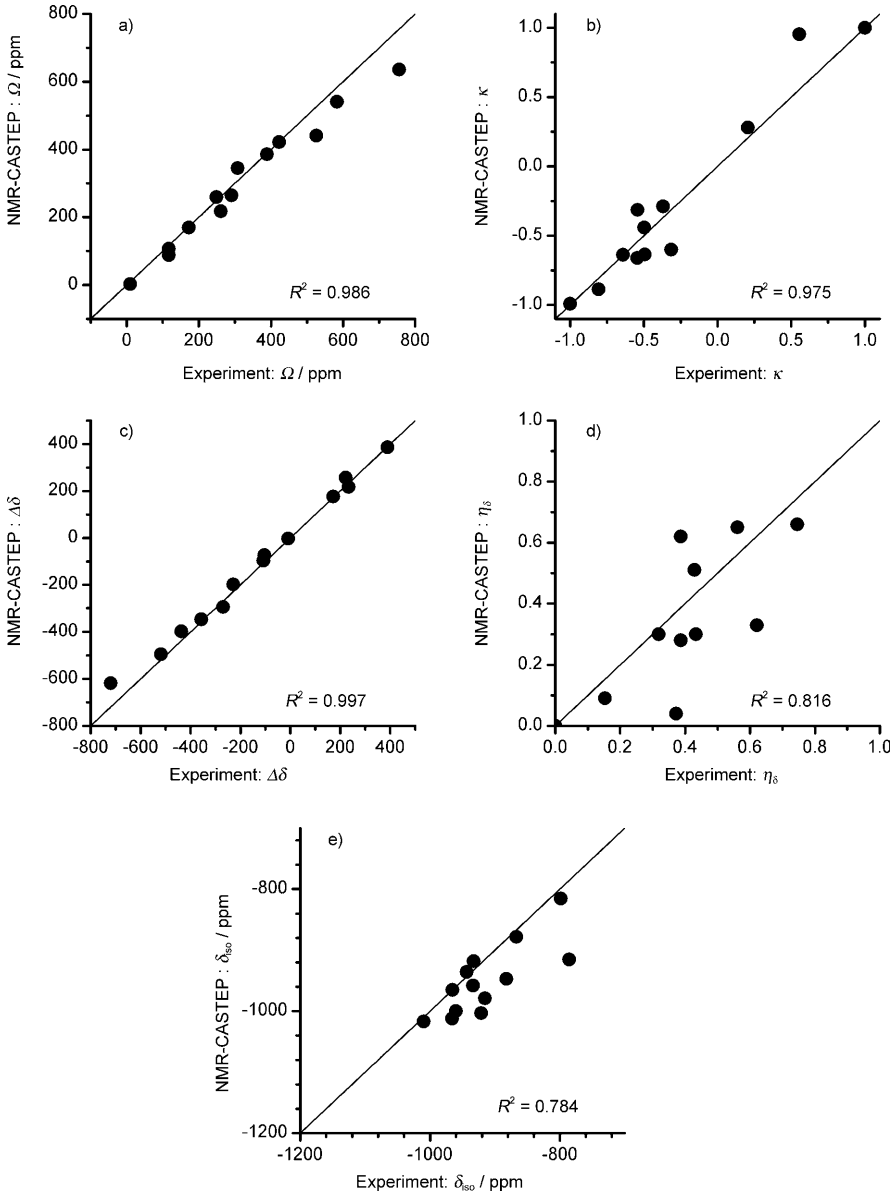

Figure 9. Graphical correlations drawn for the CS interaction parameters from a) NMR-CASTEP calculated Ω/experimentally measured Ω, b) NMR-CASTEP calculated κ/experimentally measured κ, c) NMR-CASTEP calculated $\Delta\delta$/experimentally measured $\Delta\delta$, d) NMR-CASTEP calculated η_δ/experimentally measured η_δ and e) NMR-CASTEP calculated δ_{iso}/experimentally measured δ_{iso}, for the suite of four- and six-coordinate niobate systems studied in this work.

ing η_Q, in comparison with the lone involvement of V_{33} defining C_Q. The R^2 value of 0.840 from the NMR-CASTEP data set of Figure 8d is noticeably weaker than its WIEN2k counterpart owing to the calculated value of η_Q for $NaNbO_3$ appearing particularly disparate from the other data points. This result emphasises the complexity surrounding the $NaNbO_3$ polymorphism over wide temperature ranges and the plethora of displacive transitions that can be introduced that reduce the ABO_3 perovskite structure from ideal cubic symmetry. Furthermore, many reported structures may only be partially complete and their description of long-range order could be deficient. Powder X-ray crystallography studies (not shown) of the commercial $NaNbO_3$ sample studied in this work confirms that it is the pure *Pbcm* phase reported in early work by Sakowski-Cowley et al.,[93] and it is clearly not identified with phases such as *P2ma*[97] and *Pbma*[99] reported in more contemporary work. This is corroborated by direct comparison of the NMR-CASTEP calculated ^{93}Nb NMR interaction parameters for the *Pbcm*, *P2ma* and *Pbma* phases with the experimentally measured values, as presented in Table 2. As observed through association with the δ_{iso} and C_Q values, the *Pbcm* phase is the most likely phase described by these parameters. The resultant forces on the Nb positions in the energy minimisation procedure remain high (>0.2 eV/Å) in the *Pbcm*, *P2ma* and *Pbma* studies, and full geometry optimisations to relax these reported (and often controversial) structures need to be incorporated in the methodology adopted here. This is outside the scope of this initial work and will be reported elsewhere. Nevertheless, the displaced η_Q parameter in Figure 8d suggests that the pseudopotential and all-electron approaches of NMR-CASTEP and WIEN2k, respectively, are capturing subtly different aspects of the $NaNbO_3$ electron density, and indeed may also be reflecting incompletely described/solved structural characteristics in the *Pbcm* phase. Of particular note are the direct comparisons made between the WIEN2k and NMR-CASTEP methods for the computation of C_Q and η_Q parameters in Figure 8e and f, respectively. These very high quality correlations ($R^2=0.999$ and 0.997 (0.936 if $NaNbO_3$ is included)) suggest that all-electron (WIEN2k) and pseudopotential (NMR-CASTEP) plane-wave calculations yield very coherent results between themselves, and they independently appear well suited to the computation of EFG parameters for the ^{93}Nb nucleus in heavy-element dominated niobate systems.

Figure 9a–e illustrate the correlated results of NMR-CASTEP calculated and measured chemical shift parame-

ters. Particular attention is drawn to the excellent correlations between the computed and measured values of Ω ($R^2=0.986$) and $\Delta\delta$ ($R^2=0.997$) shown in Figure 9a and c, respectively, and the modest correlation demonstrated by the analogous relationship for δ_{iso} ($R^2=0.784$) shown in Figure 9e. NMR shift parameters are strongly influenced by core and valence electronic interactions in spatial regions proximate to the nucleus where they experience the strong nuclear potential and possess large angular momentum.[109,118] This situation is particularly crucial for heavy elements because fully relativistic calculations are required to compensate for all electronic characteristics as they approach the velocity of light in these specific atomic regions. However, the recent versions of the NMR-CASTEP chemical shift calculation are restricted to scalar relativistic corrections for the core electrons only. Yates et al. have demonstrated the success of a zeroth-order regular approximation (ZORA) coupled with the pseudopotential approach for heavy elements, and this work noted that scalar relativistic corrections to the total shielding essentially cancel when relative (or chemical) shifts are considered.[109] It is yet to be tested whether the extension of scalar relativistic corrections to the valence states can indeed improve the correlation for δ_{iso} illustrated in Figure 9e. In contrast, it is noted with great interest that parameters such as Ω and $\Delta\delta$ defined by differences in shift tensor elements appear to exhibit an efficient elimination of computational corrections/errors, as evidenced by Figure 9a and c. The excellent CSS and CSA correlations described here support the methodology of the ^{93}Nb line-shape acquisition and deconvolution techniques implemented for the detection of these $\Omega/\Delta\delta$ parameters, and in addition, support the conclusion that all measurements reported in Table 2 for these niobates are realistic and accurate.

Corresponding Gaussian 03 calculations for the niobates under study here are summarised in Table 4, and the graphical correlations drawn from these data are shown in Figures 10 and 11. Unlike the WIEN2k and NMR-CASTEP approaches discussed above, the Gaussian 03 method is not a single calculation but a matrix of methods in which the user can define the overall computational method, the electronic basis set to be implemented and the method of termination used within the periodic lattice, because ultimately a discrete cluster or structural entity must be submitted for calculation. In this study of niobate systems, the most appropriate computational approaches involve RHF and B3LYP methods,[78,79] with all-electron basis sets (either 16s10p7d(5s2) or 16s10p7d(5s1)) being used for the Nb positions and the 6-311++G** basis set used for all lighter atoms.[80] A similar methodology was previously employed in a joint Gaussian 03/NMR-CASTEP study of the effectiveness of computing the ^{51}V quadrupole parameters for the lighter V^V positions in a large suite of vanadates.[102] This study demonstrated that both methods exhibited useful predictive capabilities, with Gaussian 03 performing marginally better in accurately calculating the reduced C_Q magnitudes and ranges characterising V^V systems. For Nb^V the situation is reversed as the scatter in the correlations described in Figure 10a–d show that the Gaussian 03 RHF and B3LYP approaches (irrespective of basis set) do not perform as well as their WIEN2k and NMR-CASTEP counterparts in these heavier systems. The same description is also extended to the Gaussian 03 calculation of η_Q (see Figure 11a–d) in which the correlations are poor and the scatter in these data has become acute. This performance is not unexpected because the WIEN2k and NMR-CASTEP methods take full account of the crystal structure, long-range periodicity and positional symmetries, and they both incorporate some level of relativistic correction to the core electronic states which is absent

Table 4. Experimentally measured and Gaussian calculated ^{93}Nb EFG interaction parameters for various niobate systems.

Niobate system	Experimental		Gaussian 03 source[a]							
	C_Q [MHz] (±0.03)	η_Q (±0.003)	RHF/5s2/6-311++G** C_Q [MHz]	RHF/5s2/6-311++G** η_Q	RHF/5s1/6-311++G** C_Q [MHz]	RHF/5s1/6-311++G** η_Q	B3LYP/5s2/6-311++G** C_Q [MHz]	B3LYP/5s2/6-311++G** η_Q	B3LYP/5s1/6-311++G** C_Q [MHz]	B3LYP/5s1/6-311++G** η_Q
$YNbO_4$	82.23	0.381	81.61	0.798	98.81	0.311	77.80	0.495	81.66	0.427
$LaNbO_4$	86.55	0.186	68.06	0.340	76.03	0.249	80.95	0.428	83.88	0.415
$CaNb_2O_6$	50.40	0.787	55.02	0.808	51.74	0.928	56.51	0.726	57.85	0.657
$MgNb_2O_6$	53.81	0.248	53.37	0.169	50.08	0.338	51.92	0.443	67.45	0.450
La_3NbO_7	50.87	0.212	46.68	0.228	48.27	0.168	62.78	0.934	58.85	0.939
$Mg_4Nb_2O_9$	45.55	0.000	35.90	0.000	41.82	0.000	28.87	0.001	32.97	0.001
$SnNb_2O_6$	40.06	0.477	57.55	0.108	58.61	0.049	42.10	0.747	43.70	0.674
$BiNbO_4$	20.83	0.534	21.82	0.502	22.45	0.598	22.96	0.564	17.12	0.368
$Cd_2Nb_2O_7$	24.79	0.000								
$CsBiNb_2O_7$	24.06	0.473	32.27	0.505	36.08	0.363	22.88	0.750	23.14	0.813
$LiNbO_3$	22.25	0.000	26.40	0.000	20.21	0.001	17.52	0.002	19.98	0.000
$NaNbO_3$	19.96	0.785	19.29	0.337	21.66	0.444	13.88	0.272	16.25	0.186
$KNbO_3$	22.99	0.822	12.00	0.918	21.04	0.762	22.85	0.641	20.26	0.510
Bi_3NbO_7	ca. 22.0	–	–	–	–	–	–	–	–	–
$Sn_2Nb_2O_7$	ca. 18.7	–	–	–	–	–	–	–	–	–

[a] Source from Gaussian 03 calculations is in the form 'method/Nb basis set/all other atoms basis set'.

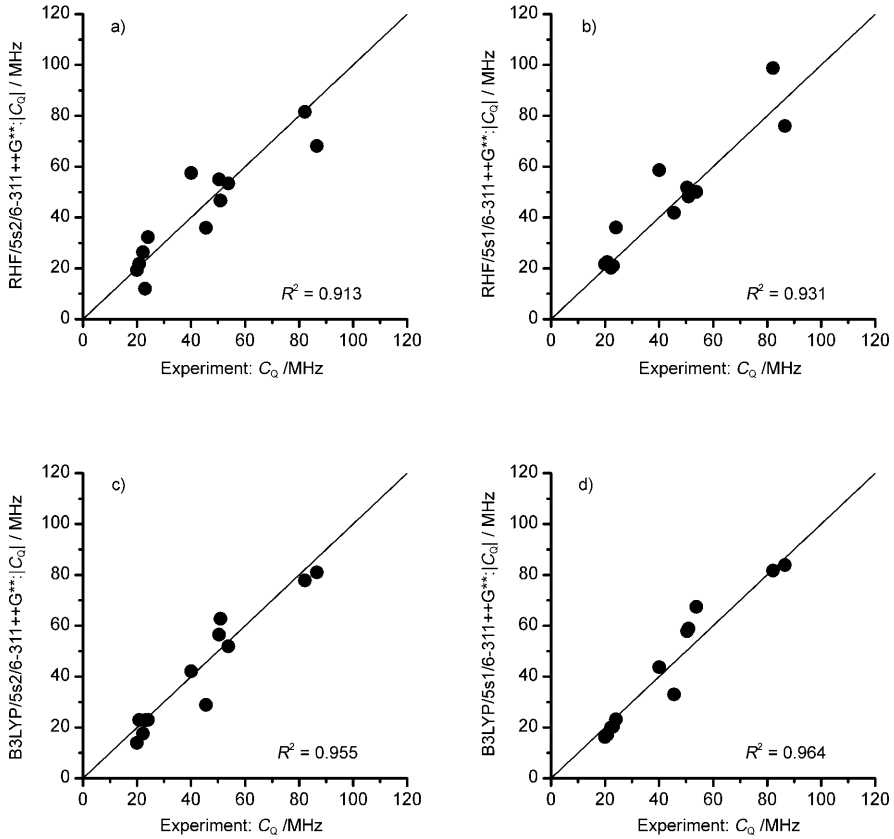

Figure 10. Graphical correlations drawn for the EFG interaction parameters from a) Gaussian 03 RHF/5s2/6-311++G** calculated $|C_Q|$/experimentally measured C_Q, b) Gaussian 03 RHF/5s1/6-311++G** calculated $|C_Q|$/experimentally measured C_Q, c) Gaussian 03 B3LYP/5s2/6-311++G** calculated $|C_Q|$/experimentally measured C_Q and d) Gaussian 03 B3LYP/5s1/6-311++G** calculated $|C_Q|$/experimentally measured C_Q for the suite of four- and six-coordinate niobate systems studied in this work.

in Gaussian 03. These properties become more important as the interactions between the heavier elements in these systems become prominent, and where the immediate Nb^V oxo coordination sphere characteristics alone cannot adequately rationalise the NMR interactions being measured (as mentioned above).

A useful indicator of the dominance of these longer-range interactions not being captured by the Gaussian 03 approach in these heavy-element studies rests with the empirically formulated shear strain and longitudinal strain parameters.[119] These local parameters are a quantitative analysis correlating the measured quadrupolar parameters and the structural distortions from the immediate coordination environment. The shear strain ($|\psi|$) is defined in [Eq. (13)] in which θ_i and θ_o are the actual and ideal O–Nb–O bond angles, respectively (i.e., $\theta_o = 109.5°$ for ideal tetrahedral coordination and $\theta_o = 90°$ for ideal octahedral coordination).

$$|\psi| = \sum_i |\tan(\theta_i - \theta_o)| \qquad (13)$$

Longitudinal strain ($|\alpha|$) is defined in [Eq. (14)] in which l_i and l_o are the actual and ideal Nb–O bond lengths, respectively. The ideal bond length is that in a perfect tetrahedron or octahedron that has the same volume as the actual coordination polyhedron in the structure under consideration.

$$|\alpha| = \sum_i \left|\ln\left(\frac{l_i}{l_o}\right)\right| \qquad (14)$$

Previous studies have reported linear relationships between C_Q and the shear and longitudinal strain parameters for a variety of lighter NMR-active nuclei including ^{23}Na,[120] ^{25}Mg,[121,122] ^{27}Al,[123,124] ^{49}Ti,[125,126] ^{65}Cu[127] and ^{91}Zr.[128,129] As evidenced from the data presented in Figure 12a and b, the total suite of four- and six-coordinate niobates shows no tendency to correlate (linearly or otherwise) with $|\psi|$ and $|\alpha|$, respectively, as both data sets describe a random scatter. However, if subgroups defined by the cationic charge and structural similarity are identified (as depicted on each diagram), then some important correlations and groupings become apparent. The most dramatic manifestation of longer-range interactions between heavy nuclei influencing the measured ^{93}Nb quadrupolar parameters is observed for the four-coordinate $LaNbO_4$ and $YNbO_4$ (depicted by the symbol ▲) systems. They clearly exhibit the largest C_Q values, yet they are characterised by smaller $|\psi|$ and $|\alpha|$ values, immediately suggesting that the heavy La^{III} and Y^{III} cations must be anisotropically influencing the Nb^V centres in the modestly distorted Nb–O tetrahedra. More conventional correlations can be established for the six-coordinate monovalent alkali perovskites (represented by the symbol ●) and the divalent systems (represented by the symbol □), although the lines merely delineate a trend and do not imply linear behaviour. Figure 12a and b shows that an encircled subgroup of the divalent systems comprised of the alkaline earth columbites ($CaNb_2O_6$ and $MgNb_2O_6$), foordite ($SnNb_2O_6$) and hexagonal $Mg_4Nb_2O_9$ are amongst the most structurally distorted octahedra from both the shear strain and longitudinal strain perspectives. Conversely, the C_Q values that characterise these systems are only mid-range in magnitude, however the ^{93}Nb CSS/CSA line-width contributions for systems such as the columbites are very sizeable ($\Omega > 500$ ppm). The most interesting member of the six-coordinate suite is the $CsBiNb_2O_7$ system (depicted

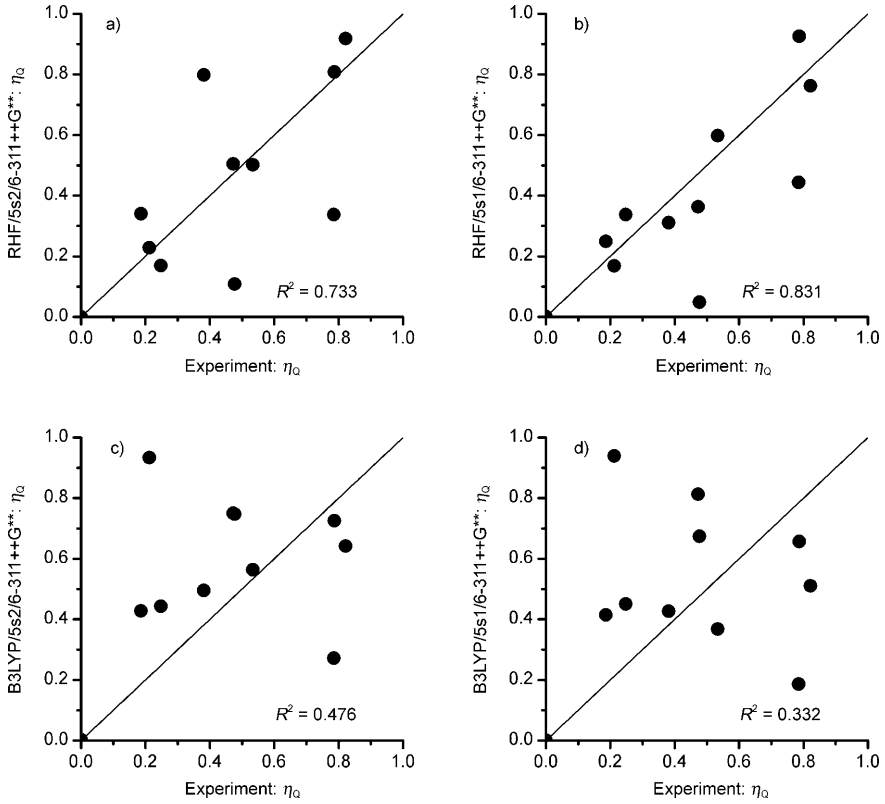

Figure 11. Graphical correlations drawn for the EFG interaction parameters from a) Gaussian 03 RHF/5s2/6-311++G** calculated η_Q/experimentally measured η_Q, b) Gaussian 03 RHF/5s1/6-311++G** calculated η_Q/experimentally measured η_Q, c) Gaussian 03 B3LYP/5s2/6-311++G** calculated η_Q/experimentally measured η_Q and d) Gaussian 03 B3LYP/5s1/6-311++G** calculated η_Q/experimentally measured η_Q for the suite of four- and six-coordinate niobate systems studied in this work.

by the symbol ◇), which possesses the most distorted oxo environment, but also exhibits a low-range C_Q value proximate to the other monovalent alkali systems. In contrast, the proximity of this Nb^V site to two large ionic radii species such as Cs^I and Bi^{III} of net cationic charge +4 induces a very anisotropic deshielding that produces the largest CSS/CSA contribution value of this suite with $\Omega > 750$ ppm. These observations, enabled through the empirical structural parameters $|\psi|$ and $|\alpha|$, illustrate that the ^{93}Nb NMR parameter determinants for these niobates is a complex combination of the immediate oxo coordination sphere and the more distant next-nearest-neighbour environment, which may include heavy cationic species.

The largely uncorrelated behaviour of the total niobate suite shown in Figure 12a and b is augmented with the additional study shown in Figure 12c, which analyses δ_{iso} as a function of mean Nb–O distance (or ⟨Nb–O⟩) for each Nb^V environment. Commensurate with the absence of any overall trend as observed above, this study also fails to identify a continuous correlation involving δ_{iso} that applies collectively to these niobate systems. It readily shows that the isotropic chemical shifts for the four-coordinate $LaNbO_4$ and $YNbO_4$ systems are well separated from the remaining six-coordinate systems, which are correlated with a noticeably smaller ⟨Nb–O⟩ distance of >0.1 Å. An increase in coordination number from four to six results in a lengthening of the Nb–O bond; this weakens the covalent bonding character so that less electron density resides at the Nb^V position resulting in an upfield shift (to lower frequency) of the ^{93}Nb resonance. Moreover, the ⟨Nb–O⟩ distance for the six-coordinate systems cluster tightly around a value of ~2.0 Å, and these characteristics do not engender a smooth monotonic δ_{iso}/⟨Nb–O⟩ relationship as reported in previous Ca–O,[130,131] Na–O[132–134] and Cs–O[135] studies. This behaviour does, however, resemble the δ_{iso}/⟨Nb–O⟩ relationship in a recently reported study of ^{25}Mg MAS NMR and DFT study of Mg^{II} in various oxo environments.[122]

Conclusion

It has been demonstrated that high precision ^{93}Nb NMR interaction data can be elucidated from static line-shape spectra acquired from a large suite of niobates. Unlike previous assertions made about the inability to detect CSA contributions from Nb^V in almost all oxo environments,[28,29] this study has emphasised that a thorough variable B_0 approach unambiguously measures the presence of both quadrupolar and CSA contributions from ^{93}Nb broadline data. These data reveal that the ^{93}Nb electric field gradient tensor is a particularly sensitive measure of the immediate and extended environments of the Nb^V positions, with C_Q values 0 to >80 MHz range being measured. Similarly, the δ_{iso} values (covering a ~250 ppm range) and Ω values (covering a 0 to ~800 ppm range) characteristic of these niobate systems are sensitive to structural disposition. However, their systematic rationalisation in terms of the Nb–O bond angles and distances defining the immediate Nb^V oxo enviroment is complicated by longer-range influences usually involving other heavy elements comprising the structure. It has also been established in this study that the best global methods of analysis for the ^{93}Nb NMR interaction parameters generated here are the WIEN2k and NMR-CASTEP DFT computational approaches, which account for the short- and long-range symmetries, periodicities and interaction-potential characteristics for all elements, and in particular, the heavy elements. Even though fundamental differences exist between the im-

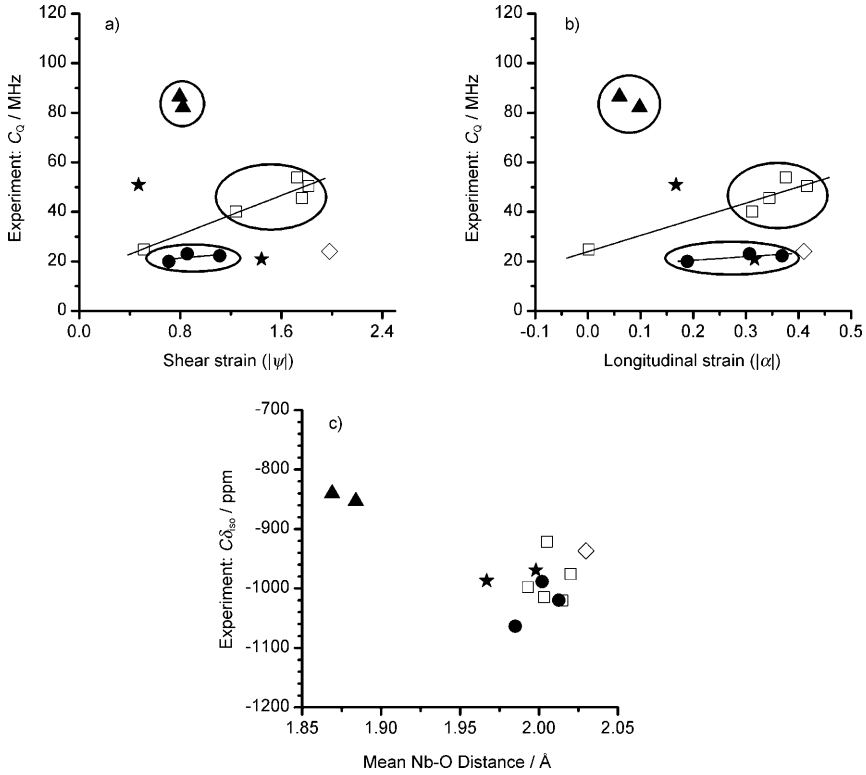

Figure 12. Graphically drawn correlations for a) experimentally measured C_Q values against the empirically derived shear strain parameter $|\psi|$, b) experimentally measured C_Q values against the empirically derived longitudinal strain parameter $|\alpha|$, and c) experimentally measured δ_{iso} values against the mean Nb–O distance. The four-coordinate orthoniobate (fergusonite) structures = ▲, the divalent columbite, corundum, foordite and pyroniobate (pyrochlore) systems = □, the monovalent alkali perovskites = ●, the trivalent fluorite and orthorhombic $BiNbO_4$ = ★ and the layered perovskite $CsBiNbO_4$ = ◇.

plementation of the WIEN2k and NMR-CASTEP methodologies, they show a remarkable consistency in the calculation of the quadrupolar parameters C_Q and η_Q, and they show very good correlations with experimentally deduced C_Q data. In comparison, the quality of this correlation is reduced when experimental and calculated values of η_Q are evaluated. Despite the absence of fully relativistic NMR-CASTEP chemical shift calculations, excellent correlations with entities such as the chemical shift span (Ω) or chemical shift anisotropy ($\Delta\delta$) are facilitated by their reliance on the differences in chemical shift tensorial elements. WIEN2k and NMR-CASTEP computational methods have proven more reliable than the time-efficient Gaussian 03 approach, mainly owing to its reliance on terminated structures, which compromise the fully periodic and long-range structural description necessary for heavier elements. These attributes are reinforced by correlations drawn by using the empirical shear strain ($|\psi|$) and longitudinal strain ($|\alpha|$) parameters, which demonstrate that the largest C_Q values obtained from this niobate suite are obtained from the least distorted nearest neighbour oxo coordination spheres. Conversely, the niobate systems that display the greatest oxo environment distortions are usually characterised by smaller EFG and the largest CS interactions, thus implying that a complex interplay of contributions from the immediate oxo environment and the next-nearest-neighbour positions (usually heavy cation dominated) are determinants in this behaviour. The three-method approach that uses crystal structure, NMR measurement and DFT calculation as invoked in this study demonstrates that the niobate structures defining this suite (except for $NaNbO_3$) and coupled ^{93}Nb solid-state NMR measurements exhibit high accuracy and congruence, as evidenced by the excellent correlations exhibited through DFT calculation of the NMR interaction parameters such as C_Q, Ω and $\Delta\delta$.

Acknowledgements

J.V.H. would like to thank Dr E. R. Vance (Institute of Materials Engineering, ANSTO Lucas Heights) for valuable assistance and discussions pertaining to the synthesis and characterisation of the niobate suite studied in this work, and Dr J. Yates (Department of Materials, University of Oxford) for helpful discussions. J.V.H. and M.E.S. would like to thank the Engineering and Physical Sciences Research Council (EPSRC), the University of Warwick and Advantage West Midlands (AWM) for partial funding of NMR infrastructure at the University of Warwick. R.W.S. and B.E.G.L. thank the Natural Sciences and Engineering Research Council of Canada (NSERC), the Canadian Foundation for Innovation (CFI), the Ontario Innovation Trust (OIT), the University of Windsor and the Centre for Catalysis and Materials Research (CCMR) for funding. R.W.S. and B.E.G.L. would like to thank the Canadian Shared Hierarchical Academic Research Computing Network (SHARCNET) for access to cluster time and services. L.S.C. would like to thank the National Sciences and Engineering and Researches Council of Canada (NSERC) for postdoctoral fellowship funding.

[1] R. W. Berg, *Coord. Chem. Rev.* **1992**, *113*, 1–130.
[2] K. Tanabe, S. Okazaki, *Appl. Catal. A* **1995**, *133*, 191–218.
[3] I. Nowak, M. Ziolek, *Chem. Rev.* **1999**, *99*, 3603–3624.
[4] K. Tanabe, *Catal. Today* **2003**, *78*, 65–77.
[5] M. Ziolek, *Catal. Today* **2003**, *78*, 47–64.
[6] M. A. Banares, I. E. Wachs, R. M. Martin-Aranda, Fourth International Symposium on Group Five Compounds, Toledo, **2002**.
[7] I. E. Wachs, Fifth International Symposium on Group Five Compounds, Jiminy Peak, **2005**.
[8] V. Luca, J. V. Hanna, M. E. Smith, M. James, D. R. G. Mitchell, J. R. Bartlett, *Microporous Mesoporous Mater.* **2002**, *55*, 1–13.
[9] V. Luca, E. Drabarek, H. Chronis, T. McLeod, *J. Nucl. Mater.* **2006**, *358*, 164–175.
[10] S. J. Tauster, S. C. Fung, R. T. K. Baker, J. A. Horsley, *Science* **1981**, *211*, 1121–1125.

[11] R. Buffon, A. Auroux, F. Lefebvre, M. Leconte, A. Choplin, J. M. Basset, W. A. Herrmann, *J. Mol. Catal.* **1992**, *76*, 287–295.
[12] S. Prasad, P. Zhao, J. Huang, J. J. Fitzgerald, J. S. Shore, *Solid State Nucl. Magn. Reson.* **2001**, *19*, 45–62.
[13] M. Vijayakumar, G. L. Hoatson, R. L. Vold, *Phys. Rev. B* **2007**, *75*, 104104.
[14] S. Prasad, P. Zhao, J. Huang, J. J. Fitzgerald, J. S. Shore, *Solid State Nucl. Magn. Reson.* **1999**, *14*, 231–235.
[15] J. J. Fitzgerald, S. Prasad, J. Huang, J. S. Shore, *J. Am. Chem. Soc.* **2000**, *122*, 2556–2566.
[16] P. Bhattacharya, M. E. Smith, P. A. Thomas, *Phase Transitions* **2006**, *79*, 79–89.
[17] D. H. Zhou, G. L. Hoatson, R. L. Vold, *J. Magn. Reson.* **2004**, *167*, 242–252.
[18] R. L. Vold, G. L. Hoatson, M. Vijayakumar, *Phys. Rev. B* **2007**, *75*, 134105.
[19] G. L. Hoatson, D. H. H. Zhou, F. Fayon, D. Massiot, R. L. Vold, *Phys. Rev. B* **2002**, *66*, 224103.
[20] T. Cardinal, E. Fargin, G. Le Flem, M. Couzi, L. Canioni, P. Segonds, L. Sarger, A. Ducasse, F. Adamietz, *Eur. J. Solid State Inorg. Chem.* **1996**, *33*, 597–605.
[21] T. Cardinal, E. Fargin, G. Le Flem, S. LeBoiteux, *J. Non-Cryst. Solids* **1997**, *222*, 228–234.
[22] M. E. Lines, *Phys. Rev. B* **1991**, *43*, 11978–11990.
[23] S. Le Boiteux, P. Segonds, L. Canioni, L. Sarger, T. Cardinal, C. Duchesne, E. Fargin, G. Le Flem, *J. Appl. Phys.* **1997**, *81*, 1481–1487.
[24] L. Petit, I. Cardinal, J. J. Videau, F. Smektala, T. Jouan, K. Richardson, A. Schulte, *Mater. Sci. Eng. B* **2005**, *117*, 283–286.
[25] L. Petit, T. Cardinal, J. J. Videau, E. Durand, L. Canioni, M. Martines, Y. Guyot, G. Boulon, *Opt. Mater. (N.Y.)* **2006**, *28*, 172–180.
[26] A. J. Barbosa, F. A. Dias, Y. Messaddeq, S. J. L. Ribeiro, R. R. Goncalves, S. R. Luthi, A. S. L. Gomes, *J. Non-Cryst. Solids* **2006**, *352*, 3636–3641.
[27] C. R. Rambo, L. Ghussn, F. F. Sene, J. R. Martinelli, *J. Non-Cryst. Solids* **2006**, *352*, 3739–3743.
[28] O. B. Lapina, D. F. Khabibulin, K. V. Romanenko, Z. Gan, M. G. Zuev, V. N. Krasil′nikov, V. E. Fedorov, *Solid State Nucl. Magn. Reson.* **2005**, *28*, 204–224.
[29] O. B. Lapina, D. F. Khabibulin, A. A. Shubin, V. V. Terskikh, *Prog. Nucl. Magn. Reson. Spectrosc.* **2008**, *53*, 128–191.
[30] L. P. Cruz, J. M. Savariault, J. Rocha, J. C. Jumas, J. D. P. de Jesus, *J. Solid State Chem.* **2001**, *156*, 349–354.
[31] L. S. Du, R. W. Schurko, K. H. Lim, C. P. Grey, *J. Phys. Chem. A* **2001**, *105*, 760–768.
[32] L. S. Du, R. W. Schurko, N. Kim, C. P. Grey, *J. Phys. Chem. A* **2002**, *106*, 7876–7886.
[33] A. Y. Lo, T. E. Bitterwolf, C. L. Macdonald, R. W. Schurko, *J. Phys. Chem. A* **2005**, *109*, 7073–7087.
[34] A. Flambard, L. Montagne, L. Delevoye, S. Steuernagel, *Solid State Nucl. Magn. Reson.* **2007**, *32*, 34–43.
[35] H. T. Kwak, S. Prasad, T. Clark, P. J. Grandinetti, *Solid State Nucl. Magn. Reson.* **2003**, *24*, 71–77.
[36] D. Massiot, I. Farnan, N. Gautier, D. Trumeau, A. Trokiner, J. P. Coutures, *Solid State Nucl. Magn. Reson.* **1995**, *4*, 241–248.
[37] A. Medek, V. Frydman, L. Frydman, *J. Phys. Chem. A* **1999**, *103*, 4830–4835.
[38] J. T. Ash, P. J. Grandinetti, *Magn. Reson. Chem.* **2006**, *44*, 823–831.
[39] M. A. Subramanian, J. C. Calabrese, *Mater. Res. Bull.* **1993**, *28*, 523–529.
[40] M. A. Subramanian, J. Gopalakrishnan, A. W. Sleight, *Mater. Res. Bull.* **1988**, *23*, 837–842.
[41] A. Kahn-Harari, L. Mazerolles, D. Michel, F. Robert, *J. Solid State Chem.* **1995**, *116*, 103–106.
[42] H. Weitzel, H. Schrocke, *Z. Kristallogr.* **1980**, *152*, 69–82.
[43] S. Tsunekawa, T. Kamiyama, K. Sasaki, H. Asano, T. Fukuda, *Acta Crystallogr. Sect. A* **1993**, *49*, 595–600.
[44] J. P. Cummings, S. F. Simonsen, *Am. Mineral.* **1970**, *55*, 90–97.
[45] A. Castro, E. Aguado, J. M. Rojo, P. Herrero, R. Enjalbert, J. Galy, *Mater. Res. Bull.* **1998**, *33*, 31–41.
[46] K. Sreedhar, N. R. Pavaskar, *Mater. Lett.* **2002**, *53*, 452–455.
[47] L. Srisombat, S. Ananta, S. Phanichphant, *Mater. Lett.* **2004**, *58*, 853–858.
[48] H. R. Danner, R. Pepinsky, *Phys. Rev.* **1955**, *99*, 1215–1217.
[49] A. C. Kunwar, G. L. Turner, E. Oldfield, *J. Magn. Reson.* **1986**, *69*, 124–127.
[50] P. R. Bodart, J. P. Amoureux, Y. Dumazy, R. Lefort, *Mol. Phys.* **2000**, *98*, 1545–1551.
[51] D. Fenzke, D. Freude, T. Frohlich, J. Haase, *Chem. Phys. Lett.* **1984**, *111*, 171–175.
[52] E. Oldfield, H. K. C. Timken, B. Montez, R. Ramachandran, *Nature* **1985**, *318*, 163–165.
[53] P. P. Man, *J. Magn. Reson.* **1986**, *67*, 78–90.
[54] P. P. Man, *Mol. Phys.* **1990**, *69*, 337–346.
[55] S. Z. Ageev, P. P. Man, J. Fraissard, B. C. Sanctuary, *Mol. Phys.* **1997**, *91*, 75–80.
[56] J. P. Amoureux, C. Fernandez, S. Steuernagel, *J. Magn. Reson.* **1996**, *123*, 116–118.
[57] QUASAR-Solid-State NMR Simulation for Quadrupolar Nuclei, J. P. Amoureux, C. Fernandez, Lille, **1996**.
[58] J. P. Amoureux, C. Fernandez, L. Carpentier, E. Cochon, *Phys. Status Solidi A* **1992**, *132*, 461–475.
[59] WSolids NMR Simulation Package, Version 1.17.30, K. Eichele, R. E. Wasylishen, **2001**.
[60] F. Angeli, T. Charpentier, P. Faucon, J. C. Petit, *J. Phys. Chem. B* **1999**, *103*, 10356–10364.
[61] F. Angeli, J. M. Delaye, T. Charpentier, J. C. Petit, D. Ghaleb, P. Faucon, *J. Non-Cryst. Solids* **2000**, *276*, 132–144.
[62] F. Angeli, J. M. Delaye, T. Charpentier, J. C. Petit, D. Ghaleb, P. Faucon, *Chem. Phys. Lett.* **2000**, *320*, 681–687.
[63] T. Charpentier, C. Fermon, J. Virlet, *J. Chem. Phys.* **1998**, *109*, 3116–3130.
[64] A. N. Tikhonov, V. A. Arsenin in *Solution of Ill-posed Problems*, Winston & Sons, Washington, **1977**.
[65] F. Angeli, M. Gaillard, P. Jollivet, T. Charpentier, *Chem. Phys. Lett.* **2007**, *440*, 324–328.
[66] G. Czjzek, J. Fink, F. Götz, H. Schmidt, J. M. D. Coey, J. P. Rebouillat, A. Liénard, *Phys. Rev. B* **1981**, *23*, 2513–2530.
[67] B. Bureau, G. Silly, J. Y. Buzaré, C. Legein, D. Massiot, *Solid State Nucl. Magn. Reson.* **1999**, *14*, 181–190.
[68] A. Samoson, *Chem. Phys. Lett.* **1985**, *119*, 29–32.
[69] C. Jäger in *NMR Basic Principles and Progress, Vol. 31*, Springer, Berlin, **1994**, p. 135.
[70] Y. Millot, P. P. Man, *Solid State Nucl. Magn. Reson.* **2002**, *21*, 21–43.
[71] T. Anupõld, A. Reinhold, P. Sarv, A. Samoson, *Solid State Nucl. Magn. Reson.* **1998**, *13*, 87–91.
[72] A. Samoson, *J. Magn. Reson. A* **1996**, *121*, 209–211.
[73] C. J. Pickard, F. Mauri, *Phys. Rev. B* **2001**, *63*, 245101.
[74] S. J. Clark, M. D. Segall, C. J. Pickard, P. J. Hasnip, M. J. Probert, K. Refson, M. C. Payne, *Z. Kristallogr.* **2005**, *220*, 567–570.
[75] J. R. Yates, C. J. Pickard, F. Mauri, *Phys. Rev. B* **2007**, *76*, 024401.
[76] WIEN2k, An Augmented Plane-Wave Plus Local Orbitals Program for Calculating Crystal Properties, P. Blaha, K. Schwarz, G. J. H. Madsen, D. Kvasnicka, J. Luitz, Technische Universität Wien, Wien, **2001**.
[77] Gaussian 03, Revision B.03, M. J. Frisch, G. W. Trucks, H. B. Schlegel, G. E. Scuseria, M. A. Robb, J. R. Cheeseman, J. A. Montgomery, Jr., T. Vreven, K. N. Kudin, J. C. Burant, J. M. Millam, S. S. Iyengar, J. Tomasi, V. Barone, B. Mennucci, M. Cossi, G. Scalmani, N. Rega, G. A. Petersson, H. Nakatsuji, M. Hada, M. Ehara, K. Toyota, R. Fukuda, J. Hasegawa, M. Ishida, T. Nakajima, Y. Honda, O. Kitao, H. Nakai, M. Klene, X. Li, J. E. Knox, H. P. Hratchian, J. B. Cross, C. Adamo, J. Jaramillo, R. Gomperts, R. E. Stratmann, O. Yazyev, A. J. Austin, R. Cammi, C. Pomelli, J. W. Ochterski, P. Y. Ayala, K. Morokuma, G. A. Voth, P. Salvador, J. J. Dannenberg, V. G. Zakrzewski, S. Dapprich, A. D. Daniels, M. C.

Strain, O. Farkas, D. K. Malick, A. D. Rabuck, K. Raghavachari, J. B. Foresman, J. V. Ortiz, Q. Cui, A. G. Baboul, S. Clifford, J. Cioslowski, B. B. Stefanov, G. Liu, A. Liashenko, P. Piskorz, I. Komaromi, R. L. Martin, D. J. Fox, T. Keith, M. A. Al-Laham, C. Y. Peng, A. Nanayakkara, M. Challacombe, P. M. W. Gill, B. Johnson, H. Chen, M. W. Wong, C. Gonzalez, J. A. Pople, Gaussian Inc., Pittsburgh, PA, **2003**.

[78] A. D. Becke, *Phys. Rev. A* **1988**, *38*, 3098–3100.
[79] C. T. Lee, W. T. Yang, R. G. Parr, *Phys. Rev. B* **1988**, *37*, 785–789.
[80] J. Andzelm, S. Huzinaga, M. Klobukowski, E. Radzio-Andzelm, Y. Sakai, H. Tatewaki in *Gaussian Basis Sets for Molecular Calculations*, Elsevier, New York, **1984**.
[81] M. Bak, J. T. Rasmussen, N. C. Nielsen, *J. Magn. Reson.* **2000**, *147*, 296–330.
[82] R. Haugsrud, T. Norby, *Nat. Mater.* **2006**, *5*, 193–196.
[83] S. Pagola, R. E. Carbonio, J. A. Alonso, M. T. Fernandez-Diaz, *J. Solid State Chem.* **1997**, *134*, 76–84.
[84] H. J. Rossell, *J. Solid State Chem.* **1979**, *27*, 287–292.
[85] N. Kumada, K. Taki, N. Kinomura, *Mater. Res. Bull.* **2000**, *35*, 1017–1021.
[86] S. Ananta, *Mater. Lett.* **2004**, *58*, 2530–2536.
[87] A. Snedden, K. S. Knight, P. Lightfoot, *J. Solid State Chem.* **2003**, *173*, 309–313.
[88] E. N. Ivanova, A. V. Yatsenko, N. A. Sergeev, *Solid State Nucl. Magn. Reson.* **1995**, *4*, 381–385.
[89] S. E. Ashbrook, S. Wimperis, *J. Magn. Reson.* **2002**, *156*, 269–281.
[90] Y. Watanabe, T. Sota, K. Suzuki, N. Iyi, K. Kitamura, S. Kimura, *J. Phys. Condens. Matter* **1995**, *7*, 3627–3635.
[91] J. Blumel, E. Born, T. Metzger, *J. Phys. Chem. Solids* **1994**, *55*, 589–593.
[92] A. F. McDowell, M. S. Conradi, J. Haase, *J. Magn. Reson. A* **1996**, *119*, 211–218.
[93] A. C. Sakowski-Cowley, K. Lukaszewicz, H. D. Megaw, *Acta Crystallogr. Sect. B* **1969**, *25*, 851–865.
[94] A. W. Hewat, *Ferroelectrics* **1974**, *7*, 83–85.
[95] M. Ahtee, C. N. W. Darlington, *Acta Crystallogr. Sect. B* **1980**, *36*, 1007–1014.
[96] R. Vondermuhll, A. Sadel, P. Hagenmuller, *J. Solid State Chem.* **1984**, *51*, 176–182.
[97] V. A. Shuvaeva, M. Y. Antipin, S. V. Lindeman, O. E. Fesenko, V. G. Smotrakov, Y. T. Struchkov, *Ferroelectrics* **1993**, *141*, 307–311.
[98] C. N. W. Darlington, K. S. Knight, *Acta Crystallogr. Sect. B* **1999**, *55*, 24–30.
[99] H. W. Xu, Y. L. Su, M. L. Balmer, A. Navrotsky, *Chem. Mater.* **2003**, *15*, 1872–1878.
[100] V. A. Shuvaeva, M. Y. Antipin, *Kristallografiya* **1995**, *40*, 511–516.
[101] I. Abrahams, A. Kozanecka-Szmigiel, F. Krok, W. Wrobel, S. C. M. Chan, J. R. Dygas, *Solid State Ionics* **2006**, *177*, 1761–1765.
[102] F. T. Mauschick, Ph.D. Thesis, University of Wuppertal, Wuppertal, **2003**.
[103] L. Truflandier, M. Paris, F. Boucher, *Phys. Rev. B* **2007**, *76*, 035102.
[104] A. Y. H. Lo, J. V. Hanna, R. W. Schurko, *Appl. Magn. Reson.* **2007**, *32*, 691–708.
[105] M. Bühl, *Theor. Chem. Acc.* **2002**, *107*, 336–342.
[106] L. K. Sanders, W. D. Arnold, E. Oldfield, *J. Porphyrins Phthalocyanines* **2001**, *5*, 323–333.
[107] P. Zhou, S. C. F. Au-Yeung, X. P. Xu, *J. Am. Chem. Soc.* **1999**, *121*, 1030–1036.
[108] X. P. Xu, S. C. F. Au-Yeung, *J. Am. Chem. Soc.* **2000**, *122*, 6468–6475.
[109] J. R. Yates, C. J. Pickard, M. C. Payne, F. Mauri, *J. Chem. Phys.* **2003**, *118*, 5746–5753.
[110] G. Schreckenbach, T. Ziegler, *Theor. Chem. Acc.* **1998**, *99*, 71–82.
[111] M. Bühl, *Chem. Eur. J.* **1999**, *5*, 3514–3522.
[112] M. Bühl, S. Gaemers, C. J. Elsevier, *Chem. Eur. J.* **2000**, *6*, 3272–3280.
[113] M. Bühl, W. Baumann, R. Kadyrov, A. Borner, *Helv. Chim. Acta* **1999**, *82*, 811–820.
[114] W. Leitner, M. Bühl, R. Fornika, C. Six, W. Baumann, E. Dinjus, M. Kessler, C. Kruger, A. Rufinska, *Organometallics* **1999**, *18*, 1196–1206.
[115] K. J. Ooms, K. W. Feindel, M. J. Williams, R. E. Wasylishen, J. V. Hanna, K. J. Pike, M. E. Smith, *Solid State Nucl. Magn. Reson.* **2005**, *28*, 125–134.
[116] A. Rodriguez-Fortea, P. Alemany, T. Ziegler, *J. Phys. Chem. A* **1999**, *103*, 8288–8294.
[117] T. M. Gilbert, T. Ziegler, *J. Phys. Chem. A* **1999**, *103*, 7535–7543.
[118] T. Gregor, F. Mauri, R. Car, *J. Chem. Phys.* **1999**, *111*, 1815–1822.
[119] S. Ghose, T. Tsang, *Am. Mineral.* **1973**, *58*, 748–755.
[120] B. Zhou, B. L. Sherriff, J. S. Hartman, G. Wu, *Am. Mineral.* **2007**, *92*, 34–43.
[121] K. J. D. Mackenzie, R. H. Meinhold, *Am. Mineral.* **1994**, *79*, 250–260.
[122] L. S. Cahill, J. V. Hanna, A. Wong, J. C. C. Freitas, J. R. Yates, R. K. Harris, M. E. Smith, *Chem. Eur. J.* **2009**, *15*, 9785–9798.
[123] M. Body, C. Legein, J. Y. Buzare, G. Silly, P. Blaha, C. Martineau, F. Calvayrac, *J. Phys. Chem. A* **2007**, *111*, 11873–11884.
[124] G. Engelhardt, W. Veeman, *J. Chem. Soc. Chem. Commun.* **1993**, 622–623.
[125] P. A. Thomas, A. Baldwin, R. Dupree, P. Blaha, K. Schwarz, A. Samoson, Z. H. Gan, *J. Phys. Chem. B* **2004**, *108*, 4324–4331.
[126] D. Padro, A. P. Howes, M. E. Smith, R. Dupree, *Solid State Nucl. Magn. Reson.* **2000**, *15*, 231–236.
[127] G. A. Bowmaker, J. V. Hanna, F. E. Hahn, A. S. Lipton, C. E. Oldham, B. W. Skelton, M. E. Smith, A. H. White, *J. Chem. Soc. Dalton Trans.* **2008**, 1710–1720.
[128] S. Sham, G. Wu, *Can. J. Chem.* **1999**, *77*, 1782–1787.
[129] Z. Yan, C. W. Kirby, Y. N. Huang, *J. Phys. Chem. C* **2008**, *112*, 8575–8586.
[130] Z. Lin, M. E. Smith, F. E. Sowrey, R. J. Newport, *Phys. Rev. B. Condens. Matter Mater. Phys.* **2006**, *69*, 224107.
[131] A. Wong, A. P. Howes, R. Dupree, M. E. Smith, *Chem. Phys. Lett.* **2006**, *427*, 201–205.
[132] A. Wong, G. Wu, *J. Phys. Chem. A* **2000**, *104*, 11844–11852.
[133] A. Wong, S. Sham, S. Wang, G. Wu, *Can. J. Chem.* **2000**, *78*, 975–985.
[134] V. Luca, C. S. Griffith, J. V. Hanna, *Inorg. Chem.* **2009**, *48*, 5663–5676.
[135] X. Xue, J. F. Stebbins, *Phys. Chem. Miner.* **1993**, *20*, 297–307.

Received: June 10, 2009
Revised: November 2, 2009
Published online: February 5, 2010

